zCOSMOS 20k

Kovac, K.; Lilly, S. J.; Knobel, C.; Bschorr, T. J.; Peng, Y.; Carollo, C. M.; Contini, T.; Kneib, J-P; Le Fevre, O.; Mainieri, V.

Published in:
Monthly Notices of the Royal Astronomical Society

DOI:
10.1093/mnras/stt2241

Publication date:
2014

Monthly Notices
of the
ROYAL ASTRONOMICAL SOCIETY

MNRAS **438,** 717–738 (2014)
Advance Access publication 2013 December 14

doi:10.1093/mnras/stt2241

zCOSMOS 20k: satellite galaxies are the main drivers of environmental effects in the galaxy population at least to $z \sim 0.7$

K. Kovač,[1]★ S. J. Lilly,[1] C. Knobel,[1] T. J. Bschorr,[1] Y. Peng,[1] C. M. Carollo,[1] T. Contini,[2,3] J.-P. Kneib,[4] O. Le Févre,[4] V. Mainieri,[5] A. Renzini,[6] M. Scodeggio,[7] G. Zamorani,[8] S. Bardelli,[8] M. Bolzonella,[8] A. Bongiorno,[9] K. Caputi,[10] O. Cucciati,[11] S. de la Torre,[12] L. de Ravel,[12] P. Franzetti,[7] B. Garilli,[7] A. Iovino,[11] P. Kampczyk,[1] F. Lamareille,[2,3] J.-F. Le Borgne,[2,3] V. Le Brun,[4] C. Maier,[13] M. Mignoli,[8] P. Oesch,[14]† R. Pello,[2,3] E. Perez Montero,[2,3,15] V. Presotto,[11,16] J. Silverman,[17] M. Tanaka,[17,18] L. Tasca,[4] L. Tresse,[4] D. Vergani,[8,19] E. Zucca,[8] H. Aussel,[20] A. M. Koekemoer,[21] E. Le Floc'h,[20] M. Moresco[22] and L. Pozzetti[8]

[1]*Institute for Astronomy, ETH Zurich, CH-8093 Zurich, Switzerland*
[2]*Institut de Recherche en Astrophysique et Planétologie, CNRS, 14, avenue Edouard Belin, F-31400 Toulouse, France*
[3]*IRAP, Université de Toulouse, UPS-OMP, Toulouse, France*
[4]*Laboratoire d'Astrophysique de Marseille, CNRS/Aix-Marseille Université, 38 rue Frédéric Joliot-Curie, F-13388 Marseille cedex 13, France*
[5]*European Southern Observatory, Karl-Schwarzschild-Str. 2, D-85748 Garching b. Muenchen, Germany*
[6]*INAF-Osservatorio Astronomico di Padova, Vicolo dell'Osservatorio 5, I-35122 Padova, Italy*
[7]*INAF-IASF Milano, via Bassini 15, I-20133 Milano, Italy*
[8]*INAF Osservatorio Astronomico di Bologna, via Ranzani 1, I-40127 Bologna, Italy*
[9]*Max Planck Institut für Extraterrestrische Physik, D-84571 Garching b. Muenchen, Germany*
[10]*Kapteyn Astronomical Institute, University of Groningen, PO Box 800, NL-9700 AV Groningen, the Netherlands*
[11]*INAF Osservatorio Astronomico di Brera, via Brera 28, I-20159 Milan, Italy*
[12]*Institute for Astronomy, University of Edinburgh, Royal Observatory, Edinburgh EH93HJ, UK*
[13]*University of Vienna, Department of Astronomy, Tuerkenschanzstrasse 17, A-1180 Vienna, Austria*
[14]*UCO/Lick Observatory, University of California, Santa Cruz, CA 95064, USA*
[15]*Instituto de Astrofisica de Andalucia, CSIC, Apartado de correos 3004, E-18080 Granada, Spain*
[16]*Dipartimento di Fisica dell' Università degli Studi di Trieste - Sezione di Astronomia, via Tiepolo 11, I-34143 Trieste, Italy*
[17]*Kavli Institute for the Physics and Mathematics of the Universe, Todai Institutes for Advanced Study, the University of Tokyo, Kashiwa 277-8583, Japan (Kavli IPMU, WPI)*
[18]*Institute for the Physics and Mathematics of the Universe (IPMU), University of Tokyo, Kashiwanoha 5-1-5, Kashiwa, Chiba 277-8568, Japan*
[19]*INAF-IASF Bologna, Via P. Gobetti 101, I-40129 Bologna, Italy*
[20]*Laboratoire AIM Paris-Saclay, UMR 7158, (CEA/IRFU - CNRS/INSU - Université Paris Diderot), CE Saclay, Bat 709, F-91191 Gif-sur-Yvette, France*
[21]*Space Telescope Science Institute, Baltimore, MD 21218, USA*
[22]*Dipartimento di Fisica e Astronomia, Universitá degli Studi di Bologna, V.le Berti Pichat, 6/2, I-40127 Bologna, Italy*

Accepted 2013 November 17. Received 2013 November 17; in original form 2013 July 16

ABSTRACT

We explore the role of environment in the evolution of galaxies over $0.1 < z < 0.7$ using the final zCOSMOS-bright data set. Using the red fraction of galaxies as a proxy for the quenched population, we find that the fraction of red galaxies increases with the environmental overdensity δ and with the stellar mass M_*, consistent with previous works. As at lower redshift, the red fraction appears to be separable in mass and environment, suggesting the action of two processes: mass $\epsilon_{\rm m}(M_*)$ and environmental $\epsilon_\rho(\delta)$ quenching. The parameters describing these appear to be essentially the same at $z \sim 0.7$ as locally. We explore the relation between red fraction, mass and environment also for the central and satellite galaxies separately, paying close attention to the effects of impurities in the central-satellite classification and using

★ E-mail: kovac@phys.ethz.ch
† Hubble Fellow.

carefully constructed samples well matched in stellar mass. There is little evidence for a dependence of the red fraction of centrals on overdensity. Satellites are consistently redder at all overdensities, and the satellite quenching efficiency, $\epsilon_{\rm sat}(\delta, M_*)$, increases with overdensity at $0.1 < z < 0.4$. This is less marked at higher redshift, but both are nevertheless consistent with the equivalent local measurements. At a given stellar mass, the fraction of galaxies that are satellites, $f_{\rm sat}(\delta, M_*)$, also increases with overdensity. The obtained $\epsilon_\rho(\delta)/f_{\rm sat}(\delta, M_*)$ agrees well with $\epsilon_{\rm sat}(\delta, M_*)$, demonstrating that the environmental quenching in the overall population is consistent with being entirely produced by a satellite quenching process at least up to $z = 0.7$. However, despite the unprecedented size of our high-redshift samples, the associated statistical uncertainties are still significant and our statements should be understood as approximations to physical reality, rather than physically exact formulae.

Key words: galaxies: evolution – galaxies: groups: general – galaxies: star formation – galaxies: statistics – cosmology: observations.

1 INTRODUCTION

Correlations between various galaxy properties and their environments have been known for many years (e.g. Hubble 1939; Oemler 1974; Davis & Geller 1976; Dressler 1980) and have now been measured up to redshifts of about $z = 1-1.5$ (e.g. Balogh et al. 2004; Hogg et al. 2004; Kauffmann et al. 2004; Blanton et al. 2005; Cucciati et al. 2006, 2010; Cooper et al. 2007, 2010; Kovač et al. 2010b; Chuter et al. 2011; Quadri et al. 2012). Of particular interest for this paper are the processes which evidently lead to the effective cessation, or 'quenching', of star formation in some galaxies. This process, or processes, moves galaxies out of the star-forming main-sequence population and produces passive red galaxies which have little or no continuing star formation. We will refer to the fraction of galaxies that have been quenched in this way, as the red fraction.

In a purely empirical approach to quantify the roles of stellar mass and environment in the evolution of galaxies, Peng et al. (2010) showed that, at $z \sim 0$, the differential effects of stellar mass and environment in the quenching of galaxies are independent of each other, in the sense that the red fraction, i.e. the fraction of galaxies that have been quenched at a given stellar mass and at a given environmental overdensity, may be written as a separable function of these two parameters. Peng et al. (2010) demonstrated that this separability is maintained in the Sloan Digital Sky Survey (SDSS; York et al. 2000) sample over three decades in the ∼1 Mpc scale environmental overdensity, and over two decades in stellar mass at $z \sim 0$. Peng et al. (2010) argued that this separability implied the action of two distinct processes, one linked to stellar mass but not environment, called 'mass quenching' and the other linked to environment but not mass, 'environmental quenching'.

Various physical processes have been suggested which would operate only in dense environments (see e.g. Boselli & Gavazzi 2006 for an extensive discussion). Among these are strangulation, in which part or all of the hot gas halo is stripped and the fuel for the future star formation of a new satellite galaxy is removed (Larson, Tinsley & Caldwell 1980; Balogh & Morris 2000; Balogh, Navarro & Morris 2000; Feldmann, Carollo & Mayer 2011). In the case of a galaxy travelling through a sufficiently dense intracluster medium, external pressure may remove even the cold gas in the stellar disc, a process commonly referred to as ram pressure stripping (Gunn & Gott 1972; Abadi, Moore & Bower 1999). Both strangulation and ram pressure stripping will suppress future star formation of a satellite galaxy, eventually transforming galaxies from blue to red and in the case of a spiral galaxy causing the visibility of spiral arms to fade. Strangulation is expected to affect star formation on the time-scales of a few, to more than 10 Gyr, (McCarthy et al. 2008), while the ram pressure stripping should quench star formation on a shorter time-scale, i.e. tens of Myr (Abadi et al. 1999; Quilis, Moore & Bower 2000), where the latter time-scale does not take into account the eventual presence of a hot gaseous halo. Moreover, Rasmussen, Ponman & Mulchaey (2006) have shown that the removal of cold galactic gas can occur also in environments with a lower intramedium density, such as groups, but on a much longer time-scale increased by up to two orders of magnitude. Satellites can also experience tidal stripping (e.g. Read et al. 2006), and their morphologies can be modified by the cumulative effect of tidal forces due to multiple close encounters between galaxies, in the so-called harassment process (Farouki & Shapiro 1981; Moore, Lake & Katz 1998). Mergers of galaxies are also expected to be more frequent in dense environments, but this would be expected to reverse at the highest densities due to the high velocity dispersions. According to the semi-analytical models, the merger rate is 4–20 times higher in regions with a high number overdensity of galaxies than in regions with a ∼100 times lower number overdensity (Jian, Lin & Chiueh 2012).

It is clear from the list above that, from a theoretical point of view, the majority if not all of the environmental differences in the overall galaxy population may be caused by the transformation of galaxies after they infall into a larger halo, i.e. after they become a satellite. For years, such theoretical predictions were observationally hard to test as the galaxy-environment studies were based on the local density of galaxies used as an environment indicator (starting from the seminal work of Dressler 1980) or they were based on comparing galaxies in and out of dense structures. Only with the advent of the large spectroscopic surveys such as SDSS at $z \sim 0$ (York et al. 2000) and zCOSMOS at $z < 1$ (Lilly et al. 2007, 2009) it has become possible to reliably separate galaxies into centrals and satellites over a broad range of galaxy and halo masses. In a growing number of papers, it has been demonstrated that the observations at $z \sim 0$ support the scenario in which environment specific processes indeed act primarily on galaxies upon their infall into a larger halo: at the same stellar mass, satellite galaxies are on average redder and more concentrated than the central galaxies (van den Bosch et al. 2008) while late-type satellites have smaller radii, larger

concentration, lower surface brightness and redder colours than the late-type centrals (Weinmann et al. 2009). About 40–50 per cent of previously blue galaxies at any stellar mass transform to red galaxies after being accreted into a larger halo and becoming a satellite (van den Bosch et al. 2008; Peng et al. 2012). This fraction also increases with increasing overdensity and/or decreasing group-centric radius (Peng et al. 2012; Wetzel, Tinker & Conroy 2012).

One could also imagine that environmental effects could also affect the properties of central galaxies, especially if the cooling of gas on to the central galaxy is linked to the mass of the surrounding halo (e.g. White, Jones & Forman 1997; McDonald, Veilleux & Mushotzky 2011). Peng et al. (2012) showed that, at $z \sim 0$, satellite quenching is sufficient to explain the bulk of the observed environmental dependence of the red fraction in the overall population of galaxies, at least when the local overdensity of galaxies is used as a proxy for environment. In other words, to first order, while all galaxies experience mass quenching, only satellites experience the effects of environmental quenching. Such statements cannot of course be exact, but rather should be taken as good approximations to an underlying, no doubt complex, reality.

Given the close coupling between the stellar and halo mass for central galaxies, it is difficult to unambiguously separate the effects of these two masses. Mass quenching could therefore conceivably also be an environmental effect. Several authors (e.g. Woo et al. 2013) have pointed out that, at fixed stellar mass, the red fraction of centrals increases with the halo mass. This however can be explained as a residual effect of the continued increase of dark mass, but not stellar mass, after a galaxy has been quenched (see Lilly et al. 2013, for details). There is also evidence (Peng et al. 2010) that the stellar mass function of passive galaxies is modestly altered by subsequent merging in high-density environments, producing small changes in the overall mass function of galaxies (Bolzonella et al. 2010) and perturbing the precise separability in red fraction that might otherwise be expected.

At higher redshifts, the picture is less clearly defined, simply because of the absence, until recently, of sufficiently large samples of galaxies with quantitative environment measures. Peng et al. (2010) suggested from an initial analysis of the first half of the zCOSMOS-bright survey that separability was maintained to $z \sim 1$ (see also similar result by Raichoor & Andreon 2012) and that the differential effects of stellar mass and environment, i.e. the mass and environmental quenching efficiencies were also more or less constant. Analysis of the full zCOSMOS-bright group catalogue (Knobel et al. 2012a) indicated that, to $z \sim 0.8$ satellites continue to be redder than centrals of the same mass, with the satellite quenching being, as at low redshift, independent of stellar mass. The mean value of the satellite quenching efficiency $\epsilon_{\rm sat}$ (averaged over all overdensities) has the same value out to $z \sim 0.8$ as locally, i.e. $\epsilon_{\rm sat} \sim 0.5$ (Knobel et al. 2013, see also Quadri et al. 2012; van der Burg et al. 2013).

The aim of this paper is to construct the red fraction–environment relation up to $z = 0.7$ using the final so-called '20k' sample of the zCOSMOS-bright galaxies and to understand its origin in terms of the central-satellite dichotomy. In particular, we wish to critically test, with a larger data set and with a more sophisticated treatment of potential systematic effects, whether the relations expected from the formalism of Peng et al. (2010, 2012), which are derived mostly in the local SDSS sample, continue to hold at these higher redshifts. Previous studies of environmental effects in the zCOSMOS sample have addressed the dependence of colour (Cucciati et al. 2010; Iovino et al. 2010; Knobel et al. 2013), morphology (Tasca et al. 2009; Kovač et al. 2010b), stellar mass function (Bolzonella et al. 2010), X-ray detected AGNs (Silverman et al. 2009), infrared-luminous galaxies (Caputi et al. 2009), radio-emitting galaxies (Bardelli et al. 2010), post-starburst galaxies (Vergani et al. 2010) and close pairs (Kampczyk et al. 2013) on environment (Knobel et al. 2009, 2012a; Kovač et al. 2010a). Using only photometric redshifts, Scoville et al. (2007b, 2013) extended the environment reconstruction in the COSMOS field up to $z = 3$.

The layout of the paper is as follows. We introduce the data set and the derived products needed for the analysis in Section 2. In Section 3, we measure the relation between the red fraction of all galaxies and their environments and, in Section 4, we investigate the equivalent relations that are obtained when separating the population of galaxies into centrals and satellites. A comparison between different environment estimators and with previous results is presented in Section 5. Final conclusions are presented in Section 6. The bulk of the analysis is carried out using the red galaxies as an approximation for the quenched population. We show in Appendix C that all our statements remain valid when using the colour–colour diagram to select quenched galaxies.

A concordance cosmology with $\Omega_{\rm m} = 0.25$, $\Omega_\Lambda = 0.75$ and $H_0 = 70$ km s^{-1} Mpc^{-1} is assumed throughout. Magnitudes are given in the AB system. We use the term 'dex' to express the antilogarithm, so 0.1 dex corresponds to a factor of 1.259.

2 DATA

2.1 zCOSMOS survey

zCOSMOS (Lilly et al. 2007, 2009) is a redshift survey conducted in the 2 deg^2 area of the large legacy *Hubble Space Telescope* (*HST*) programme COSMOS (Scoville et al. 2007a). The observations were carried out using the VIMOS spectrograph (Le Fèvre et al. 2003) on the 8 m VLT/UT3 telescope spread over 600 h of service dark time. As a part of the zCOSMOS campaign, the spectra of about 20 000 galaxies down to $I_{AB} < 22.5$ were obtained over the whole COSMOS field producing a sample in the redshift range $z < 1.2$ (zCOSMOS-bright). In addition, about 10 000 targets in the inner 1 deg^2 were selected by a combination of the colour–colour criteria aimed to select galaxies in $1.8 < z < 3$ (zCOSMOS-deep).

In this paper, we use galaxies with reliable redshifts from the final, so-called 20k, zCOSMOS-bright spectroscopic catalogue. We first remove galaxies with either no redshift or with a not completely reliable spectroscopic redshift that is inconsistent with the photometrically estimated redshift range. Specifically, confidence classes 0, 1.1–1.4, 2.1, 9.1, and also the secondary and broad-line objects with corresponding confidence classes (see Lilly et al. 2007, 2009 for a description) are removed, leaving us with 17 042 objects with reliable redshifts. On average, a sampling rate of ∼50 per cent of the parent population (combining the spatial sampling rate and the redshift success rate) is achieved (e.g. Knobel et al. 2012a) with the redshift uncertainty about 100 km s^{-1}.

2.2 Photometric redshifts and properties of galaxies

2.2.1 Photometric redshifts

The targeted COSMOS field has a multitude of follow-up photometric observations by a range of ground-based and spaced-based facilities covering the UV-NIR range (e.g. Capak et al. 2007), and the *Spitzer* IRAC bands (Sanders et al. 2007). The large amount of multiwavelength data and the precision of the *HST* Advanced

Camera for Surveys data are utilized to derive state-of-the-art photometric and structural properties of all zCOSMOS galaxies.

Although the primary analysis in this paper is based on the spectroscopic sample, we use the photometric redshifts (both the photometric redshift probability distribution function, i.e. PDF(z), and the maximum likelihood photometric redshift) of COSMOS galaxies at two points in the paper (see Sections 2.3 and 2.4). These photometric redshifts were generated using ZEBRA+ (Oesch et al. 2010; Knobel et al. 2012a), which is an extension of the ZEBRA code (Feldmann et al. 2006). This code is based on fitting spectral energy distribution (SED) templates to the photometric data allowing both maximum likelihood and Bayesian approaches. The photometric redshifts which we use are obtained from the Bayesian ZEBRA+ run based on the Bruzual & Charlot (2003) models with emission lines, using the template correction module of ZEBRA based on a randomly selected subset of zCOSMOS spectroscopic redshifts. The fitting is carried out on the 26 photometric bands ranging from the Canada–France–Hawaii Telescope u^* to the *Spitzer* IRAC 4.5 μm, where 12 of the used bands are broad, 12 bands are intermediate and 2 bands are narrow. The uncertainty of the photometric redshifts is $0.01(1 + z)$ with a catastrophic failure rate of 2–3 per cent.

2.2.2 *Stellar masses and luminosities*

The same code is also utilized to derive stellar masses M_* and luminosities of all zCOSMOS galaxies but using only the 12 broad-band filters and the Bruzual & Charlot (2003) templates without emission lines, assuming the Chabrier (2003) initial stellar mass function (IMF) and Calzetti et al. (2000) dust model. The redshift of a galaxy is fixed to the spectroscopic one for galaxies with reliable spectroscopic redshifts, otherwise the maximum likelihood photometric redshift is used. It should be noted that the stellar masses which we use are obtained by integrating the past star formation rate (SFR) and they include the mass of gas processed by stars and returned to the interstellar medium (this is different than in the previous results by our group based on the 10 k zCOSMOS sample). This approach is particularly useful when comparing quiescent galaxies over different redshifts, as their masses will remain the same. On average, the total integrated stellar masses are higher by about 0.2 dex than the stellar masses with the mass return subtracted.

2.2.3 *Colour and SFR bimodality*

The rest-frame $U - B$ colour versus stellar mass diagrams of the zCOSMOS 20k galaxies in $0.1 < z < 0.4$ and $0.4 < z < 0.7$ are shown in Fig. 1 in the top and bottom panels, respectively. The continuous line corresponds to our adopted division of galaxies into blue and red (consistent with no redshift evolution in the colour division cut, mirroring Knobel et al. 2013). The division is somewhat arbitrary, as there is no clear separation between the blue and red galaxies in our data, i.e. when plotting the colour histogram in narrow bins of mass the minimum in the histogram does not show a clear trend with the mass (probably also due to the small numbers of galaxies). The division which we use is such that the blue cloud galaxies are below this division line and a slope of the dividing line is similar to the slope of red sequence galaxies.

We will use red galaxies as a proxy for the quenched population as it is measured in a simple well-defined way for all zCOSMOS galaxies. As has often been pointed out, a weakness of this approach is that the presence of dust in star-forming galaxies will redden galaxies and may put some of the dusty star formers into the population of the colour-defined quenched galaxies.

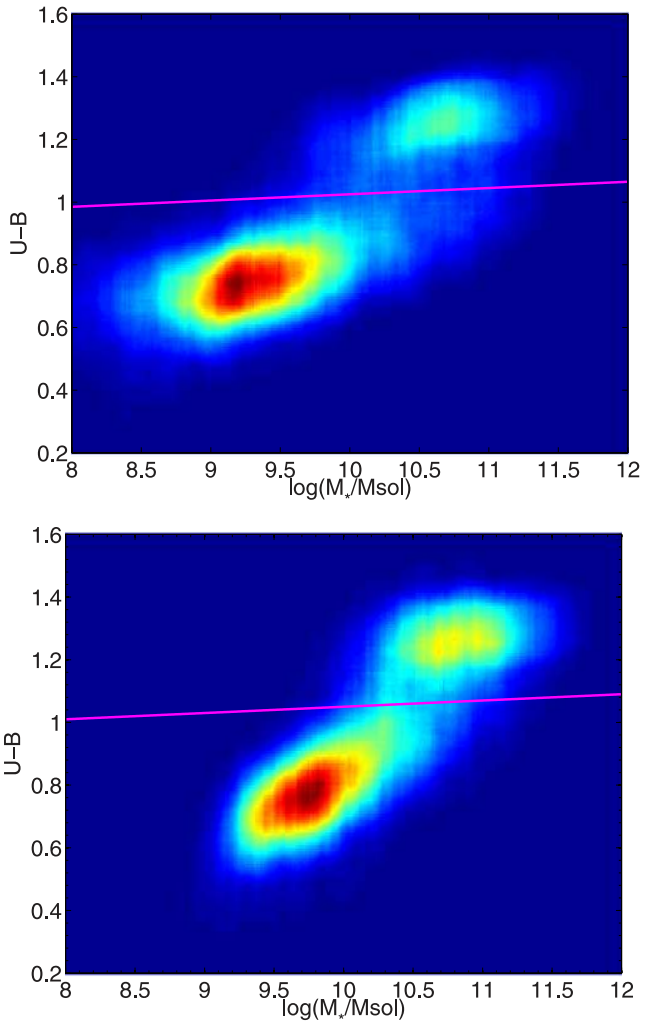

Figure 1. Rest-frame $U - B$ colour versus stellar mass for zCOSMOS galaxies in $0.1 < z < 0.4$ (top) and $0.4 < z < 0.7$ (bottom). Panels are colour-coded according to the numbers of galaxies calculated in a sliding box $\Delta(U - B) = \Delta\log(M_*/\mathrm{M}_\odot) = 0.2$ with a step of 0.01 in both parameters. The continuous line marks the adopted division between the blue and red galaxies. In this work, we will refer to all galaxies above the division line as red (i.e. quenched).

To understand the influence of the different selection criteria for the quenched population, we first look at the fraction of (colour-selected) red and (SFR-selected) non-star-forming galaxies, and compare these as a function of stellar mass. For this, we used an SFR derived from IR+UV, for galaxies detected in 24 μm, and, otherwise, an SFR derived from the SED fit. There is good agreement between these two estimators, while the emission line [O II]-based SFR shows a rather large scatter with the other two SFR measurements. We use the 24 μm data down to $S_{24\,\mu\mathrm{m}} \geq 80$ μJy obtained from the *Spitzer* observations (Le Floc'h et al. 2009). The total IR luminosity is measured following Wuyts et al. (2011) and, combining it with the UV from the SED fit, the total SFR is calculated following Kennicutt (1998) assuming Chabrier (2003) IMF.

The SFR-stellar mass plots are shown in the lower two panels in each part of Fig. 2, where the continuous line is used to separate star-forming and non–star-forming (quenched) galaxies, following the division by Knobel et al. (2013). We colour-code galaxies

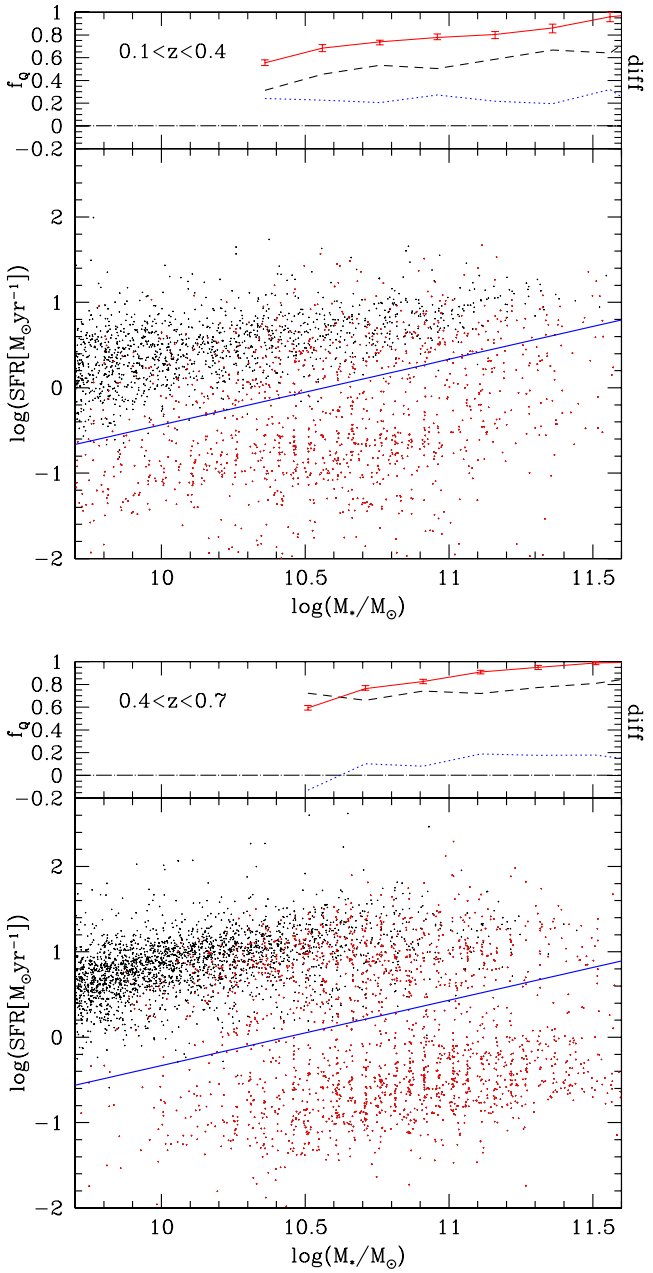

Figure 2. Difference in selecting the quenched population of galaxies by colour and by SFR in $0.1 < z < 0.4$ (top figure) and $0.4 < z < 0.7$ (bottom figure). The SFR-stellar mass relations are shown in the bottom panels, marking in red those galaxies that are classified as quenched according to the colour criterion. The continuous lines correspond to the adopted division between star-forming and non-star-forming galaxies. The quenched fractions of galaxies f_Q from the two approaches are shown in the top panels, separating galaxies by colour (red continuous lines) and by SFR (black dashed lines). The difference between these two derived fractions is shown as the blue dotted line. Finally, the long-dash–dotted line marks the zero value. The error bars are estimated by bootstrapping (16–84 per cent interval) and for clarity they are shown only for the red fractions.

classified to be red according to the previously discussed colour criterion. As expected, some of the red galaxies lie on the star-forming sequence. This is quantified in the top panels, where we show the fraction of red (continuous lines) and non-star-forming (dashed lines) galaxies, as well as the difference in these fractions (dotted lines) as a function of stellar mass. We show only the points where the red galaxies are complete above 40 per cent with respect to the fully sampled deeper, photometric data set (mass completeness will be discussed in Section 2.3; here we do not correct the measured fractions for the incompleteness in stellar mass). While the red fractions defined by colour are systematically higher than the fractions of non-star-forming galaxies (except for one point), the difference is not a strong function of stellar mass. The difference is constant at about 20 per cent in $0.1 < z < 0.4$, and it changes from 15–19 per cent in $0.4 < z < 0.7$, ignoring the lowest mass bin at higher redshift where there is a higher fraction of non-star-forming than red galaxies, but where mass incompleteness is also highest. We suspect that the apparent weak mass dependence in the difference between the two fractions in $0.4 < z < 0.7$ is a result of the change in SFR tracer among lower mass non-star-forming galaxies, as we are complete only to about $\log(\mathrm{SFR}[\mathrm{M}_\odot\ \mathrm{yr}^{-1}]) = 0.4$ for the IR+UV measurement in this redshift bin. The IR+UV-based SFR tends to empty the so-called green valley in the colour–mass diagram and to decrease the fraction of non-star-forming galaxies. We conclude that even though there are systematic differences in the fractions of quenched galaxies when defined by colour and by SFR, they are almost independent of stellar mass, and therefore, qualitatively our conclusions should be also applicable when separating galaxies by their SFR.

Finally, we note that there are many other ways to define the quenched population of galaxies (discussed extensively in the case of zCOSMOS in Moresco et al. 2013), and one needs to take care of these differences when comparing results reported in the literature. The colour–colour selection is one of the commonly used diagnostic tools to separate dusty star-forming and quiescent galaxies (e.g. Williams et al. 2009; Bundy et al. 2010; Ilbert et al. 2010, 2013). To enable a quantitative comparison with results from such works, we will also repeat some of the key parts in our analysis using the $(\mathrm{NUV} - r) - (r - J)$ diagram to identify the quenched galaxies. These colour–colour derived results are presented in Appendix C. Although the fractions of quenched galaxies selected by the colour–colour diagram are systematically lower than the equivalent fractions obtained by the $U - B$ colour cut (similar to the results shown in Fig. 2), all of our conclusions drawn when using the red fractions remain qualitatively unchanged when using the $(\mathrm{NUV} - r) - (r - J)$ selected quiescent galaxies.

2.3 Mass completeness

To understand the mass completeness in the zCOSMOS sample, we make use of the available, much deeper, photometric data. For this purpose, we use an independently estimated catalogue with photometric redshifts, masses and luminosities of COSMOS galaxies down to $I_{AB} = 24$ which was also generated using the ZEBRA+ code. The completeness is calculated as the fraction of zCOSMOS $I_{AB} < 22.5$ galaxies with reliable spectroscopic redshifts in the sample of $I_{AB} < 24$ galaxies, as a function of stellar mass in the zCOSMOS sampled area. The $I_{AB} < 24$ sample can be assumed to be complete at the masses of interest (e.g. fig. 8 in Ilbert et al. 2010). We calculate the completeness separately for the red and blue galaxies in the two redshift bins in consideration. It should be noted that by comparing the final reliable spectroscopic sample of the zCOSMOS galaxies to the overall $I_{AB} < 24$ sample, we also take into account the effects of any residual incompleteness stemming from any dependence of the ability to obtain a spectroscopic redshift on the galaxy colour or luminosity, even those are in principle small (figs 2 and 3 in Lilly et al. 2009 for the 10k zCOSMOS).

Throughout this paper, we use the inverse of this completeness $w_c(M_*, z, U-B)$ to weight galaxies with spectroscopic redshifts in order to correct for the colour-dependent mass-incompleteness. Furthermore, we only consider masses above a certain mass-completeness limit, taken (for both blue and red) to be the mass where the zCOSMOS red galaxies reach 30 per cent completeness relative to the deeper $I_{AB} < 24$ sample. In $0.1 < z < 0.4$, this completeness limit is at $\log(M_*/\mathrm{M}_\odot) = 9.82$ and in $0.4 < z < 0.7$ it is at $\log(M_*/\mathrm{M}_\odot) = 10.29$.

2.4 Environmental overdensity

In this paper, we quantify environment by measuring the overdensity of tracer galaxies at the position of each galaxy in $0.1 < z < 0.7$, and with a central/satellite classification (Section 2.5). The overdensity δ is defined as

$$\delta = \frac{\rho - \bar{\rho}}{\bar{\rho}}, \quad (1)$$

where ρ is the density of tracer galaxies in a given aperture, and $\bar{\rho}$ is the mean density at the redshift of a galaxy whose environment is being measured. Kovač et al. (2010a) discuss in detail the quantification of galaxy environments, focusing particularly on the optimization of the density field reconstruction for the zCOSMOS survey. In that paper, a new algorithm ZADE was developed to take into account galaxies without spectroscopic redshifts. In essence, ZADE is based on modifying the PDF(z) of galaxies not yet observed spectroscopically by the number counts of galaxies with reliable redshifts within some spherical R_{ZADE} apertures along the line of sight. In this way, the precise RA–Dec. positions of all galaxies are preserved and, at least in a statistical sense, the mean intergalactic separation is set by the total sample of tracer galaxies, and not only by those with spectroscopic redshifts. Importantly, the possibly complicated spatial selection function is taken automatically into account. With the ZADE algorithm any of the standard density measures can be applied, resulting in the density field that is reconstructed on a smaller scale and with less noise than in the case if the galaxies without spectroscopic redshifts are included only via a statistical weighting scheme.

Following Kovač et al. (2010a), we use the ZADE algorithm to produce the modified PDF(z) of all $I_{AB} < 22.5$ galaxies in the zCOSMOS field which do not have reliable redshifts (described in Section 2.1). Although with the 20k sample, we have about twice as many galaxies with reliable redshifts than were available in the 10k sample, the spectroscopic coverage increased towards the edges of the survey area, as well as the survey's area itself and we use the same $R_{\mathrm{ZADE}} = 5\,h^{-1}$Mpc as for the density reconstruction with the 10k sample. The suitability of the adopted R_{ZADE} value was checked with mock catalogues. To measure densities, we use circular apertures defined by the distance to the fifth nearest neighbour projected within ± 1000 km s^{-1} from the sample of tracer galaxies. We use a $M_B < -19.3 - z$ set of tracer galaxies which are luminosity complete up to $z = 0.7$. These are the same sampling apertures and tracer set as used for many of the analyses with the 10k sample as well as the $z \sim 0$ SDSS analyses of Peng et al. (2010, 2012) and thereby allow direct comparison with the previous results. The mean density is obtained by adding the $\Delta V(z)/V_{\mathrm{max}}$ contribution of all tracer galaxies (both with spectroscopic and photometric redshifts) at a given redshift, following the method outlined in Kovač et al. (2010a). According to tests that were carried out on the mock catalogues from Kitzbichler & White (2007), the error interval ($\pm 1\sigma$) in such reconstructed overdensities at the positions of galaxies is in the range $-0.2 < \Delta[\log(1+\delta)] < 0.1$, without a systematic offset in $-1 < \log(1+\delta) < 0.75$, while in more dense regions the reconstructed observed overdensity is systematically lower than the true value, by about $\Delta[\log(1+\delta)] = 0.1$ at $\log(1+\delta) \approx 2$.

2.5 Group catalogue and classification of galaxies into centrals and satellites

The group catalogue employed in this work to separate centrals and satellites is taken from Knobel et al. (2012a). The final catalogue includes 1498 groups in the redshift range $0.1 \lesssim z \lesssim 1.0$. The fraction of galaxies assigned to groups decreases from 35 per cent to 10 per cent over the same redshift interval. The reconstruction is based on the flux-limited sample of galaxies with reliable redshifts, utilizing a multirun friends-of-friends algorithm as introduced in Knobel et al. (2009), where different group finding parameters are used depending on the group richness. The optimization of the group finding parameters is carried out on the Kitzbichler & White (2007) mock catalogues, but the final assessment of quality of the reconstructed groups is recalculated on the updated COSMOS cones described in Henriques et al. (2012). According to these, the zCOSMOS 20k groups have both completeness and purity of around 83 per cent (Knobel et al. 2012a). A nominal halo mass of each group is estimated using the correlation between the number of group members, corrected for the spatial sampling and for the redshift success rate, and the halo mass calibrated on the mock catalogues.

Knobel et al. (2012a) developed a scheme to separate galaxies into centrals and satellites in which, by definition, the most massive galaxy in a group is the central, and all other group galaxies are satellites. To improve the quality of the central/satellite classification, the galaxies with only photometric redshifts (down to the flux limit of the zCOSMOS sample) are also included, since there is a 50 per cent chance that the central in each group was not observed spectroscopically. The classification of a galaxy to be a central or a satellite is done in a probabilistic manner through the combination of values of parameters p and p_M. These correspond to the probability of a galaxy to be a member of a group and the probability that it is the most massive in a group. An additional parameter p_{MA} is also calculated as the probability that a galaxy is the most massive normalized by the area of the projected Voronoi cell of that galaxy. These probabilities are calibrated via mock catalogues (see Knobel et al. 2012a for more details).

Following Knobel et al. (2012a), we separate zCOSMOS galaxies into dichotomous samples of centrals and satellites identifying the satellites as galaxies satisfying the following criteria simultaneously: $p > 0.1$, $p_M < 0.5$ and $p_{MA} < 0.5$. The central galaxies are considered to be galaxies not satisfying at least one of these criteria. Such defined samples of zCOSMOS centrals and satellites in $0.1 < z < 0.8$ are complete at the level of 93 and 54 per cent, respectively, and their purities are at the level of 84 and 74 per cent, respectively (Knobel et al. 2012a). This includes the uncertainty that in the mocks the most massive galaxy in a group is not always the central galaxy.[1] Finally, the number of galaxies in different samples used in the subsequent analysis is given in Table 1.

[1] In the mocks, central galaxies (i.e. 'type 0') are not identified by their stellar mass; they are the central galaxies of main subhaloes (Guo et al. 2011).

Table 1. Galaxy samples.

$z1 < z < z2$	All	Centrals	Satellites
$0.1 < z < 0.4$	2340	1730	610
$0.4 < z < 0.7$	2448	2062	386

Number of galaxies in different samples used in the analysis. The redshift bins $z_1 < z < z_2$ are given in the first column, and the numbers of all, central and satellite galaxies above the adopted stellar mass-completeness limit in a given redshift bin are given in the second, third and fourth column, respectively.

3 COLOUR–DENSITY RELATION FOR ALL GALAXIES

3.1 Red fractions of zCOSMOS galaxies

Numerous studies, both in the local Universe and at higher redshifts, have shown that the properties of galaxies depend on both their stellar mass and on their environment (e.g. Kauffmann et al. 2003; Baldry et al. 2006; Peng et al. 2010). In order to isolate the effects of the latter, it is necessary to carefully control the selection of the sample in terms of the former, especially given the evidence that the mass function of galaxies may be different in different environments (e.g. Bolzonella et al. 2010; Kovač et al. 2010b).

In this section, we explore further the relation between the red fraction of zCOSMOS galaxies, using the red galaxies as a proxy for the quenched population, and their environment and stellar mass. In Section 4, we will split the sample into centrals and satellites. We calculate the fraction of red galaxies in bins of $\Delta\log(M_*/\mathrm{M}_\odot) = \Delta\log(1+\delta) = 0.3$ over a range of masses above the mass-completeness limits (Section 2.3) in the two redshift intervals $0.1 < z < 0.4$ and $0.4 < z < 0.7$. We weight individual galaxies by their colour-dependent mass-completeness $w_c(M_*, z, U-B)$ that was computed in Section 2.3. The statistical uncertainty range that is given by the error bars are the 16–84 per cent intervals obtained by bootstrapping the samples 100 times.

The resulting colour–density relations are shown in Fig. 3 for independent stellar mass bins. Although there is some scatter, there is a clear trend that, at a given stellar mass, the red fraction of galaxies increases with the environmental overdensity. At a given overdensity, there is also a trend for the red fraction to increase with the stellar mass (Fig. 4). These trends are consistent, but with improved statistics, with the previously published results from the smaller 10k zCOSMOS sample (Cucciati et al. 2010, see also Tasca et al. 2009 for a similar analysis based on morphologies) and are also in qualitative agreement with similar studies from other surveys up to redshifts of unity or slightly higher (e.g. Baldry et al. 2006; Cooper et al. 2010; Peng et al. 2010).

3.2 Mass and environmental quenching

It was proposed by Baldry et al. (2006) that the dependence of the red fraction on the mass M_* and environment δ at $z \sim 0$ can be quantitatively described by a separable function of the form

$$f_{\mathrm{red}}(M_*, \delta) = 1 - \exp[-(\delta/p_1)^{p2} - (M_*/p_3)^{p4}]. \quad (2)$$

Peng et al. (2010, 2012) used this separability to derive their phenomenological model of quenching in terms of two independent processes, mass quenching and environmental quenching. Using the limited zCOSMOS 10k data set in $0.3 < z < 0.6$, Peng et al. (2010) also showed that there is a good indication that such fitting formulae can describe the measured red fraction up to $z \sim 1$. We now re-examine this with the improved 20k sample.

Our best-fitting $p1-p4$ parameters are given in Table 2, using for the fit $f_{\mathrm{red}}(M_*, \delta)$ measured in the $-0.25 < \log(1+\delta) < 2$ and $M_{\mathrm{compl}}(30\,\mathrm{per\,cent}) < \log(M_*/\mathrm{M}_\odot) < 11.5$ intervals, i.e. where the environment–mass plane is well sampled by the zCOSMOS data. In the fitting procedure, we use the overdensity and stellar mass in $\log(1+\delta)$ and $\log(M_*/\mathrm{M}_\odot)$ units. The red fractions

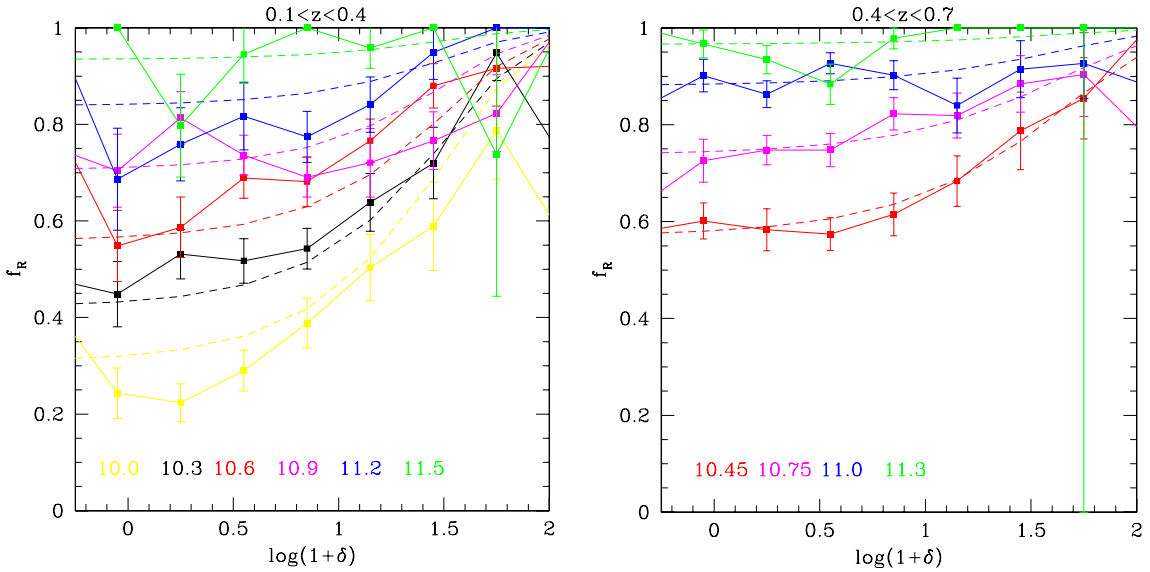

Figure 3. Red fraction as a function of overdensity in different mass bins. Results in the left- and right-hand panels are for $0.1 < z < 0.4$ and $0.4 < z < 0.7$, respectively. The measurement points connected by the continuous lines and the dashed curves are for the 0.3 dex bins in stellar mass, with the stellar mass increasing from the bottom to the top. The lowest mass bin starts at the adopted mass-completeness value in that redshift bin, and the rounded values of the centres of the used mass bins are given in the increasing order at the bottom of each panel. The symbols and the continuous lines correspond to the zCOSMOS measurements (Section 3.1), and the dashed lines correspond to the best-fitting model given by equation (2) (Section 3.2). The error bars correspond to half of the 16–84 per cent interval of the ordered red fractions from 100 bootstrapped samples in each redshift bin.

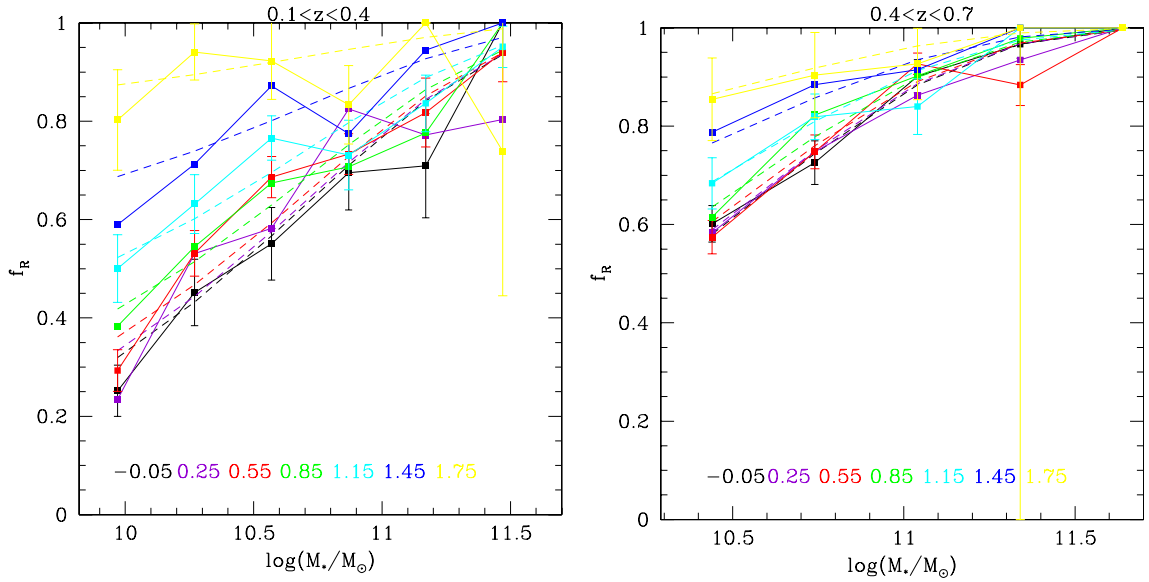

Figure 4. Red fraction as a function of stellar mass in different bins of overdensity. Results in the left- and right-hand panels are for $0.1 < z < 0.4$ and $0.4 < z < 0.7$, respectively. The measurement points connected by the continuous lines and the dashed curves correspond to the 0.3 dex bins in $\log(1+\delta)$, where the environmental overdensity increases from the bottom to the top. The values of the centres of the used environment bin, in an increasing order, are shown at the bottom of each panel. The horizontal axis starts at the adopted mass-completeness value in a given redshift bin. The symbols and the lines correspond to the zCOSMOS measurements (Section 3.1), and the dashed lines correspond to the best-fitting model given by equation (2) (Section 3.2). The error bars correspond to half of the 16–84 per cent interval of the ordered red fractions from 100 bootstrapped samples in each redshift bin, shown for clarity only for every second $\log(1+\delta)$ bin.

Table 2. Best-fitting parameters to the red fraction model.

$z1 < z < z2$	$p1$	$p2$	$p3$	$p4$
$0.1 < z < 0.4$	1.54	1.10	10.72	0.58
$0.4 < z < 0.7$	1.68	0.94	10.55	0.67

The lower z_1 and upper z_2 limits of the redshift bin to which the results refer to are given in the first column, and the best-fitting $p1$, $p2$, $p3$ and $p4$ parameters to the equation (2) are given in the second to the fifth columns. The fit is obtained with overdensity and mass expressed in $\log(1+\delta)$ and $\log(M_*/\mathrm{M}_\odot)$ units.

resulting from our best-fitting model are overplotted in Figs 3 and 4 and agree with the majority of points within 2σ. The same result is also shown in Fig. 5, where the red fraction across the (M_*, δ) plane is plotted. The colour background shows the fitted model, while the contours show the data. The differences between the modelled and observed red fractions are in the range of 5–10 per cent (in the extreme points 15 per cent). Most importantly, the residuals show no systematic trends across the (M_*, δ) plane when normalized by the uncertainties (as shown in Fig. A1 in Apendix A). We conclude that overall a separable $f_{\rm red}$ function provides a good representation of the zCOSMOS data in both the redshift intervals studied (the errors on the fit will be shown below).

As argued in Peng et al. (2010), this suggests that the red fraction is dominated by two distinct processes, one a function of mass and not environment, and the other a function of environment and not mass. This is because the blue fraction $f_{\rm blue}$, which is the chance that a galaxy has survived as a star-forming galaxy can be written as the product of two functions, one of mass alone and the other of environment alone:

$$f_{\rm blue} = 1 - f_{\rm red}(M_*, \delta) = (1 - \epsilon_\rho(\delta, \delta_0)) \times (1 - \epsilon_m(M_*, M_{*0})), \quad (3)$$

where $\epsilon_\rho(\delta, \delta_0) = 1 - \exp(-(\delta/p_1)^{p2})$ and $\epsilon_m(M_*, M_{*0}) = 1 - \exp(-(M_*/p_3)^{p4})$ (Peng et al. 2010). ϵ_ρ and ϵ_m are the so-called relative environmental quenching and mass-quenching efficiencies, respectively.

These may be calculated from the data as

$$\epsilon_\rho(\delta, \delta_0, M_*) = \frac{f_{\rm red}(\delta, M_*) - f_{\rm red}(\delta_0, M_*)}{f_{\rm blue}(\delta_0, M_*)} \quad (4)$$

and

$$\epsilon_m(M_*, M_{*0}, \delta) = \frac{f_{\rm red}(M_*, \delta) - f_{\rm red}(M_{*0}, \delta)}{f_{\rm blue}(M_{*0}, \delta)}, \quad (5)$$

where δ_0 is the overdensity at which ϵ_ρ is negligible and M_{*0} is the mass at which ϵ_m is negligible.

ϵ_ρ and ϵ_m can be interpreted as the net fraction of galaxies that has been quenched by the environment- or mass-related processes, respectively, and their functional form provides an important constraint on the physical nature of these processes. In Peng et al. (2010, 2012), it was shown that the continuity equation for galaxies plus the observed constancy of the shape of the mass function of star-forming galaxies requires that ϵ_m should have a particular form related to the faint-end slope α and the exponential cut-off M* of the Schechter-fit to the star-forming mass function and to the logarithmic slope of the SFR$-M_*$ relation of main sequence galaxies. This is different in detail from the exponential form of equation (2) which was introduced by Baldry et al. (2006) simply to describe the data. The focus of this paper is on ϵ_ρ, and we prefer to use the functional form of $\epsilon_{\rm m}$ given above with fitted $p3$ and $p4$ parameters to self-consistently define $\epsilon_{\rm m}$.

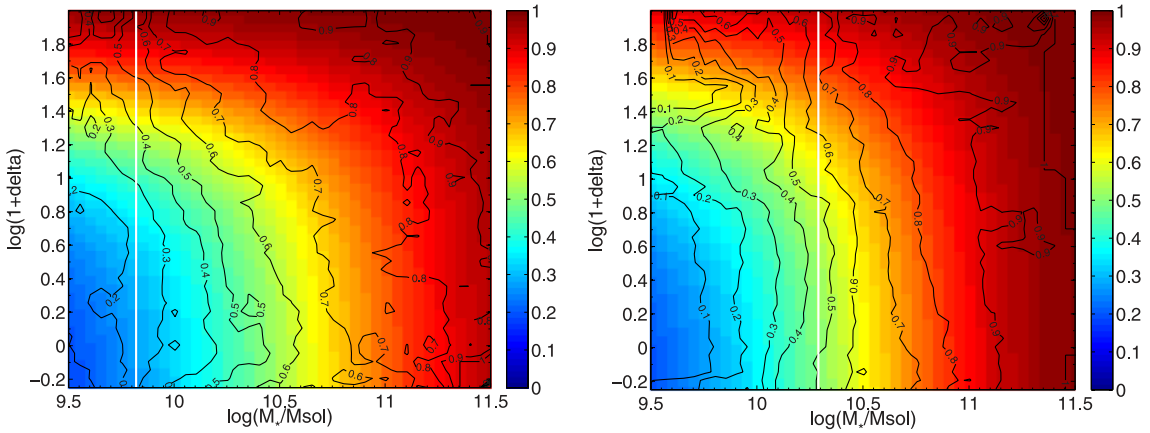

Figure 5. Red fractions from the model and from the data in the $\log(1+\delta) - \log(M_*/\mathrm{M}_\odot)$ plane. The panels are for $0.1 < z < 0.4$ and $0.4 < z < 0.7$ on the left and the right, respectively. The colour shading corresponds to the red fraction from the best-fitting model given by equation (2). The black contours correspond to the red fractions that are measured from the zCOSMOS data boxcar smoothed with the interval $\Delta\log(M_*/\mathrm{M}_\odot) = \Delta\log(1+\delta) = 0.45$ with the step 0.05 in both parameters. Such smoothing is used only for presentation purposes in this figure and it is not used in any of the calculations. The white vertical lines mark the adopted mass-completeness limits. Our analysis is based only on the data in the mass-complete area.

One of the concerns when fitting $f_{\rm red}$ over the two-dimensional overdensity–mass surface is that we are working with a relatively small number of galaxies covering a rather narrow range of stellar mass. To estimate the uncertainties on the fit (i.e. on the mass and environmental quenching efficiencies), we generate mock samples of 100 000 galaxies in each redshift bin whose distribution in mass–overdensity matches the zCOSMOS sample. Each simulated galaxy is then assigned to be red or blue according to the zCOSMOS best-fitting $p1-p4$ model. We then repeat the fitting procedure for 100 randomly chosen sub-samples that each contains the same number of galaxies as the actual zCOSMOS sample in that redshift bin. We find that there are no systematic effects due to the reduced sampling in the sense that the median ϵ_ρ and $\epsilon_{\rm m}$ functions from the 100 re-samples closely match the input functions. These 100 re-samples are then used to define the 16–84 per cent interval of the distribution of returned ϵ_ρ and $\epsilon_{\rm m}$, which are then taken as the $\pm1\sigma$ uncertainty interval on the fits returned from the actual zCOSMOS data.

We show in Figs 6 and 7 the best-fitting ϵ_ρ and $\epsilon_{\rm m}$ quenching efficiency curves in the $0.1 < z < 0.4$ and $0.4 < z < 0.7$ ranges, with the adopted error intervals estimated as above. For reference, we also show the corresponding $z \sim 0$ functions that were measured from the SDSS by Peng et al. (2010), slightly shifted in mass to account for the different definitions of mass used. Comparing the curves at different redshifts, we do not find a significant change with redshift in either the ϵ_ρ or $\epsilon_{\rm m}$ functions out to $z = 0.7$.[2] The constancy of $\epsilon_{\rm m}$ is directly related, via the continuity equation, to the observed constancy of the M* of the star-forming galaxy population (see Peng et al. 2010). The constancy of ϵ_ρ, which was also noted with our earlier data (Peng et al. 2010) is in a sense more interesting: it tells us that the physical processes responsible for the environmental differentiation of galaxies (or, at least, the environmentally caused quenching) must act in the same way as a function of overdensity over the range of epochs studied. We explore in Section 5 the links between this overdensity and other environment measurements.

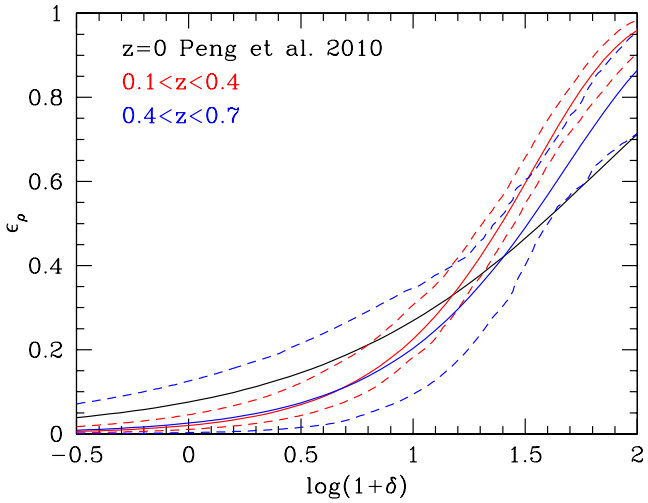

Figure 6. Redshift evolution of the ϵ_ρ function. The environmental quenching efficiencies obtained from the fit to the measured red fractions in the zCOSMOS data in $0.1 < z < 0.4$ and $0.4 < z < 0.7$ are shown as continuous lines in red and blue, respectively. The dashed lines in the same colour mark the 16–84 per cent error interval. For comparison, the ϵ_ρ function from the SDSS $z \sim 0$ data measured by Peng et al. (2010) is shown in black.

Separability will be broken if there is any quenching channel that depends on a coupling between mass and environment, or if there are ways for galaxies to e.g. change their mass differentially (e.g. through merging) in different environments. With the uncertainties in the data, we cannot rule out the presence of any such effects: our point would simply be that they must at most represent small perturbation to the simple picture implied by separability.

Finally, it should be noted that a constancy of ϵ_ρ does not imply that environmental quenching is not continuing over time. Galaxies will be migrating to denser environments and, in addition, environmental quenching must continuously operate to quench some of the lower mass galaxies whose mass increases by star formation, as discussed in Lilly et al. (2013).

[2] Peng et al. (2010) use properties of the zCOSMOS 10k galaxies estimated differently than in this work, and they adopt the redshift-evolving cut in the red/blue division of galaxies. The $\epsilon_{\rm m}$ measured from the 10k zCOSMOS data set in $0.1 < z < 1.0$ does not evolve with redshift (Peng et al. 2010), consistent with our results.

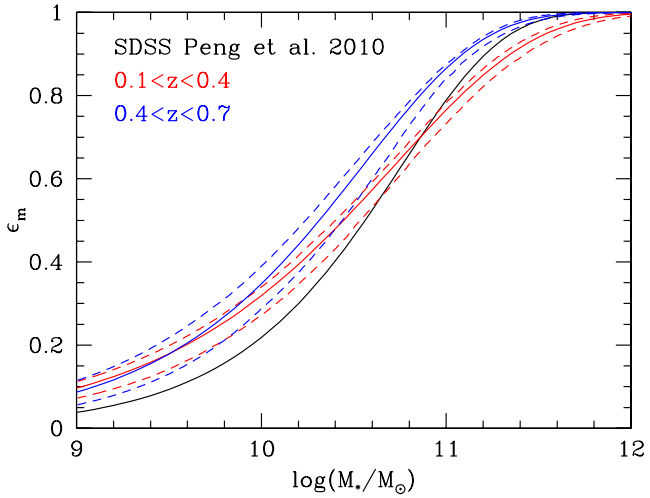

Figure 7. Redshift evolution of the ϵ_m function. The mass-quenching efficiencies obtained from the fit to the measured red fractions in the zCOSMOS data in $0.1 < z < 0.4$ and $0.4 < z < 0.7$ are shown as the continuous lines in red and blue, respectively. The dashed lines in the same colour mark the 16–84 per cent error interval. For comparison, the ϵ_m function from the SDSS $z \sim 0$ data measured by Peng et al. (2010) is shown in black. To correct for the different definition of the stellar mass used, the log ($p3$) parameter from Peng et al. (2010) is increased by 0.2.

4 CENTRAL-SATELLITE DICHOTOMY (SATELLITE QUENCHING)

4.1 Fraction of satellites in different overdensities

In this section, we investigate the overall relations between the zCOSMOS centrals and satellites and their environments defined by the nearest neighbour counts (described in Section 2.4). As a first step, we show in Fig. 8 the distribution of overdensities for the zCOSMOS centrals and satellites. As before, we consider two redshift bins, $0.1 < z < 0.4$ and $0.4 < z < 0.7$, and only galaxies above the mass-completeness limit. The satellite galaxies are systematically shifted to higher overdensity regions in both redshift bins (see also fig. 22 in Kovač et al. 2010a). Even though centrals make on average a larger fraction in the total galaxy population (fig. 1 in Knobel et al. 2013 for the zCOSMOS 20k sample), satellites become the dominant population of galaxies at the highest overdensities (green curve in Fig. 8).

In order to determine the role of centrals and satellites in shaping the overall environmental relations, we need to calculate the satellite fraction as a function of mass and overdensity, correcting the observed numbers for the mass incompleteness and for the misclassification of centrals and satellites.

Knobel et al. (2013) estimated that the purity of central-satellite classification for zCOSMOS galaxies up to $z < 0.8$ is rather high, about 80 per cent, and only weakly dependent on stellar mass. This was based on the 24 Henriques et al. (2012) mocks. Here, we use the same mocks to test whether there should be any dependence of purity on the overdensity. For simplicity, we quantify the environment around each mock galaxy (satisfying $I_{AB} < 22.5$ and $0.1 < z < 0.7$) by calculating the local overdensity of galaxies using the distance to the fifth nearest $M_B < -19.3 - z$ neighbour projected within ± 1000 km s^{-1}. By applying the same central/satellite reconstruction procedure on the mock galaxies as used for the real data (developed by Knobel et al. 2012a), we find that the purity P of the mass-complete samples of centrals and satellites is strongly

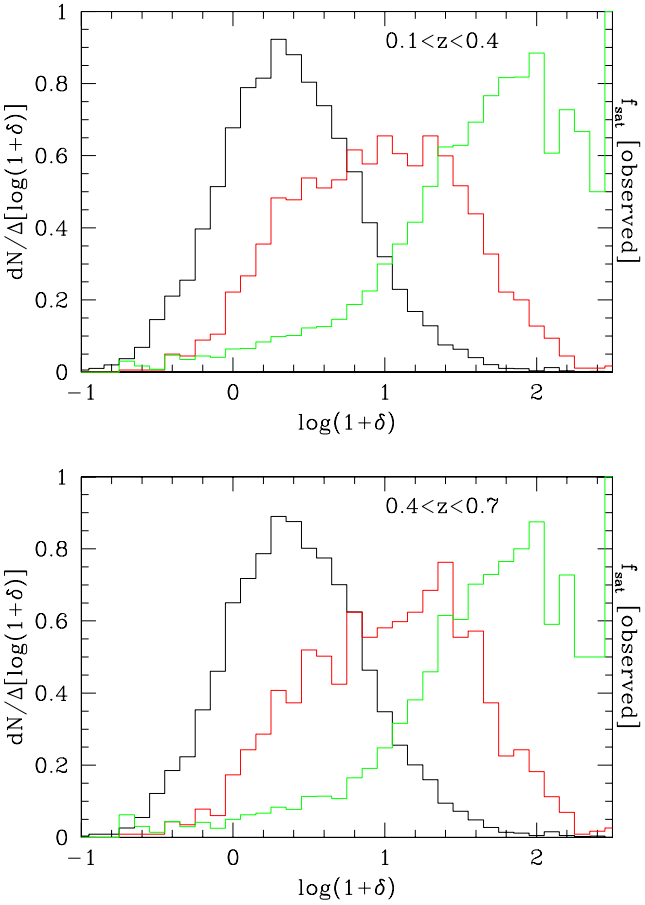

Figure 8. Overdensities of central and satellite galaxies. The distributions for the mass-complete samples in $0.1 < z < 0.4$ and $0.4 < z < 0.7$ are shown in the top and bottom panels, respectively. The black and red curves correspond to the overdensity distributions of central and satellite galaxies, respectively, normalized by their respective observed number in a given redshift bin and scaled by the bin size. The green curves correspond to the observed fraction of satellites in the total population of galaxies in a given redshift bin as a function of overdensity.

dependent on the overdensity because $f_{\rm sat}$ increases with the overdensity. This is shown in Fig. 9 for both redshift samples considered in this work. The purity of the central galaxies $P_{\rm cen}$ is more than 95 per cent in the lowest density environments, and then slowly decreases with increasing overdensity to 78 per cent at $\log(1 + \delta) = 0.65$, after which the purity sharply decreases to values of about 30–32 per cent at $\log(1 + \delta) \sim 2$. As shown in Fig. 8, there are very few centrals at these highest overdensities. This is rather obvious, as at high overdensities most galaxies are in large groups with many members, only one of which is the central. The purity of satellites $P_{\rm sat}$ shows the opposite behaviour. It is roughly constant at about 80 per cent and 70 per cent up to $\log(1 + \delta) \sim 1.25$ in the lower and higher redshift bins, respectively, and then increases to more than 90 per cent for $\log(1 + \delta) > 2$ in both redshift bins. We obtain similar results when repeating the calculation within bins of stellar mass. The strong dependence of purity on the overdensity of the reconstructed samples of centrals and satellites, and the opposite direction of this dependence, makes it imperative to correct for these impurities for any quantities measured from the observed samples of centrals and satellites.

We use these mock-estimated $P(M_*, \delta)$ purity values to calculate the 'real' fraction of satellites as a function of overdensity. For the

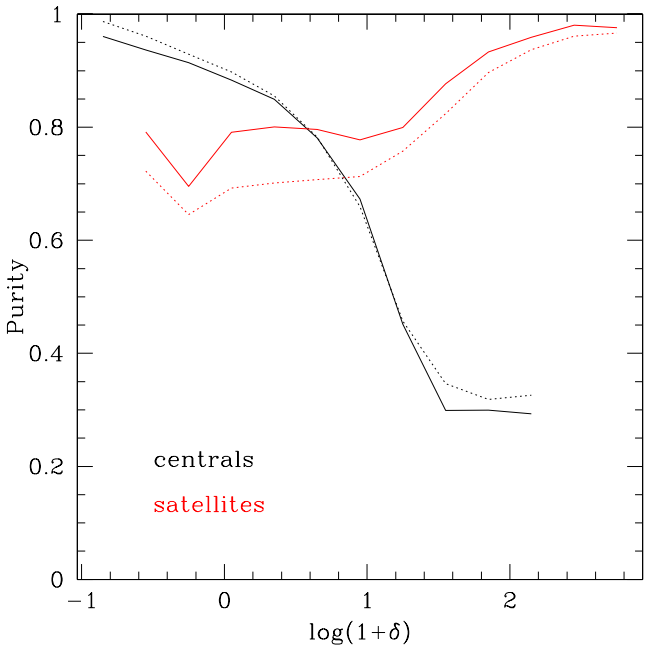

Figure 9. Purity of the central and satellite galaxies as a function of overdensity in the reconstructed mock samples. The continuous and dotted curves are for the redshift bins $0.1 < z < 0.4$ and $0.4 < z < 0.7$, respectively. The curves in black and red are the results for the central and satellite galaxies, respectively. Only the mock galaxies with stellar masses above the adopted mass-completeness limit in a given redshift bin are used.

dichotomous samples consisting of $\tilde{N}_{\rm cen}$ centrals and $\tilde{N}_{\rm sat}$ satellites (i.e. in which every galaxy in the full zCOSMOS sample is classified either a central or a satellite) the corrected (i.e. true) number of centrals $N_{\rm cen}$ and satellites $N_{\rm sat}$ can be calculated as

$$N_{\rm cen} = \tilde{N}_{\rm cen} - (1 - P_{\rm cen})\tilde{N}_{\rm cen} + (1 - P_{\rm sat})\tilde{N}_{\rm sat} \quad (6)$$

$$N_{\rm sat} = \tilde{N}_{\rm sat} - (1 - P_{\rm sat})\tilde{N}_{\rm sat} + (1 - P_{\rm cen})\tilde{N}_{\rm cen} \quad (7)$$

so that the 'real' satellite fraction is simply given as $f_{\rm sat}(M_*, \delta) = N_{\rm sat}/(N_{\rm sat} + N_{\rm cen})$. The purity-corrected fraction of zCOSMOS satellites as a function of overdensity in the $\log(M_*/{\rm M}_\odot) = 0.5$ bins is shown in Fig. 10 for the lower and higher redshift bins in the panels on the top and bottom, respectively. The error interval corresponds to the 16–84 per cent range in the satellite fractions from the 100 bootstrapped samples. Given that the central-satellite classification is dichotomous, the fraction of centrals at any overdensity is simply $1 - f_{\rm sat}(M_*, \delta)$.

Following this correction, the fractional contribution of centrals and satellites to the overall galaxy population remains a strong function of overdensity. At the lowest overdensities, more than 90 per cent of galaxies are centrals. With increasing overdensity, the fraction of satellites increases, and satellites become the dominant population at $\log(1 + \delta) \gtrsim 1$. The fraction of satellites is also a weak function of stellar mass: at a given overdensity, $f_{\rm sat}(M_*, \delta)$ decreases with stellar mass, but the difference is less than 10 per cent between the mass bins in the well-sampled range of overdensities. Moreover, our data do not indicate any strong redshift evolution in $f_{\rm sat}(M_*, \delta)$. For the 0.5 dex bin in stellar mass centred at $\log(M_*/{\rm M}_\odot) = 10.54$, which is observable in both redshift bins, we do not find an evolution in the fraction of satellites at a given overdensity between the two redshifts bins.

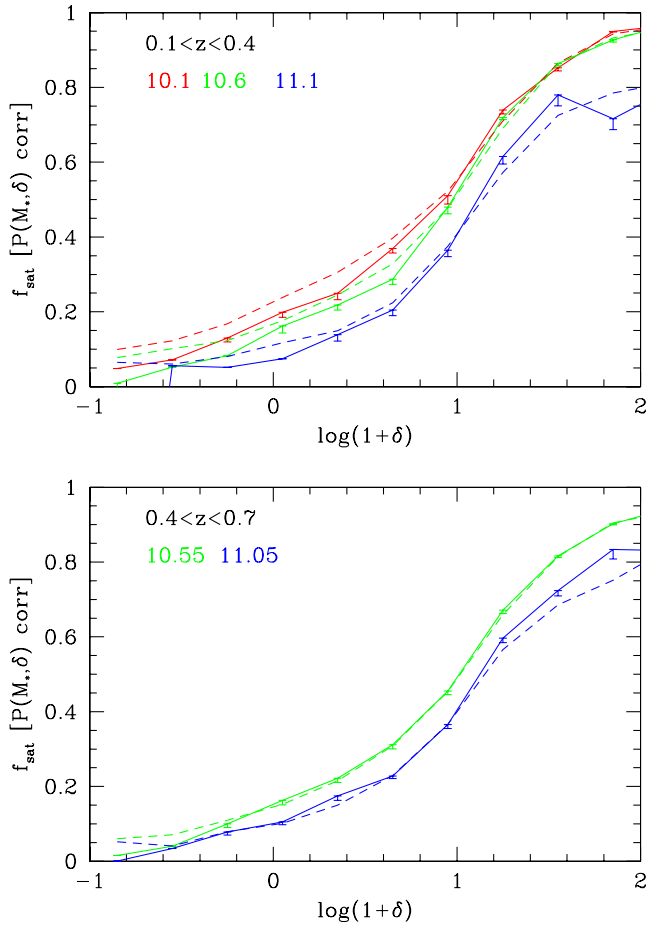

Figure 10. Fraction of satellites as a function of overdensity. The results in $0.1 < z < 0.4$ and $0.4 < z < 0.7$ are shown in the top and bottom panels, respectively. The differently coloured curves correspond to the fractions measured in 0.5 dex bins of stellar mass. The lowest mass bins start at the adopted mass-completeness limit. The rounded values of the centre of the mass bins are marked in the second row of the label in the top-left corner in the panels. The symbols (connected by the continuous lines) represent the fractions measured from the zCOSMOS data, and the dashed lines represent the equivalent fractions measured from the Henriques et al. (2012) mocks. The errors on the data points correspond to the 16–84 per cent range in the satellite fractions from the 100 bootstrapped samples. As the samples of centrals and satellites are dichotomous, the fraction of centrals at any overdensity is simply $1 - f_{\rm sat}(M_*, \delta)$.

We also compare the measured satellite fractions with the equivalent fractions in the mock catalogues. Overall, the fractions of satellites in zCOSMOS and in the mocks agree well both in the trends with the overdensity and with stellar mass. This can be seen in Fig. 10.

Peng et al. (2012) used only the mock defined $f_{\rm sat}(M_*, \delta)$ in their analysis, but the $f_{\rm sat}(M_*, \delta)$ curves in Peng et al. (2010), based on the earlier Kitzbichler & White (2007) mocks, show a weaker dependence on stellar mass. As a check, we measure the environments of $I_{AB} < 22.5$ galaxies in the Kitzbichler & White (2007) mocks, calculating the overdensities in exactly the same manner as for the Henriques et al. (2012) mocks, as part of the difference could stem from differently defined mean densities. We also find that $f_{\rm sat}(M_*, \delta)$ in the Kitzbichler & White (2007) mocks shows much weaker dependence on stellar mass, finding the decrease in $f_{\rm sat}(M_*, \delta)$ only for the highest mass $\log(M_*/{\rm M}_\odot) \sim 11.1$ bin in $0.1 < z < 0.4$.

Variations in the mass dependence of the satellite fraction inevitably introduce differences in the relationships between environmental quenching and satellite quenching effects. Not least, even a weak mass dependence of $f_{\rm sat}(M_*, \delta)$ will mean that it is not possible for both the satellite and environmental quenching efficiencies in Peng et al. (2012) to be strictly independent of mass.

4.2 Red fractions of central and satellite galaxies

In this section, we investigate the colour–density relations that are obtained when separating the overall galaxy population into central and satellite galaxies. Due to the opposite dependence of the purity on overdensity for the centrals and satellites (shown in Fig. 9), any relation between a given property and the overdensity that is measured separately for the centrals and satellites, and the differences between the two, may be strongly affected by the impurity of the central-satellite classification. We can however correct for this statistically, as the observed red fractions of centrals $\tilde{f}_{r,\rm cen}$ and satellites $\tilde{f}_{r,\rm sat}$ are related to the 'true' respective fractions $f_{r,\rm cen}$ and $f_{r,\rm sat}$ by simple relations:

$$\tilde{f}_{r,\rm sat} = P_{\rm sat} f_{r,\rm sat} + (1 - P_{\rm sat}) f_{r,\rm cen} \quad (8)$$

$$\tilde{f}_{r,\rm cen} = P_{\rm cen} f_{r,\rm cen} + (1 - P_{\rm cen}) f_{r,\rm sat}. \quad (9)$$

Using the $P_{\rm sat}$ and $P_{\rm cen}$ (as a function of mass and environment) as estimated above in Section 4.1, one can easily obtain the statistically corrected, i.e. 'true', red fractions of centrals and satellites from the observed red fractions of apparent centrals and satellites.

Ideally, we would like to carry out the analysis for the centrals and satellites in the same way as for the overall galaxy population, presented in Section 3. However, given the small number of satellites (totalling about 1000 in both redshift bins, see Table 1), the systematic shift in the overdensities occupied by the central and satellite galaxies, and the necessity to derive any quantity in the same bins for both centrals and satellites (in order to correct for the impurities), we need to modify our approach to obtain reliable results. Instead of working in narrow bins of stellar mass, we derive the red fractions of centrals and satellites as a function of overdensity in mass-matched samples.

We therefore create mass-matched samples of both centrals and satellites as follows. Starting from the sample of centrals in each of the two redshift ranges, we first divide the galaxies lying above the mass-completeness limit into four bins in overdensity, defined by the quartiles in the overdensity distribution of the mass-complete *centrals*. As a reference sample, we define a fifth bin which contains central galaxies around the median overdensity, i.e. with overdensities in the 37.5–62.5 per cent range of sorted overdensities. The (stellar) mass-matched samples are then built by randomly picking, for each galaxy in the reference sample, one galaxy from each of the four overdensity quartiles which is chosen to have a stellar mass close to the stellar mass of the reference galaxy. To obtain an estimate of the uncertainties we repeat this process 20 times. More details of the matching process and the (weighted) stellar mass distributions of the matched samples are given in Appendix B.

Using the adopted colour cut, we then measure the red fraction of centrals at the median weighted stellar mass in the matched samples in the four overdensity bins. The median mass is $\log(M_*/{\rm M}_\odot) = 10.47$ and 10.71 in the lower and higher redshift bins, respectively. We then combine equations (8) and (9) to correct for impurity, calculating $\tilde{f}_{r,\rm sat}$ using the satellites that reside in the same range of overdensities and within the 0.75 dex mass interval centred on the median mass of the central galaxies. This approach

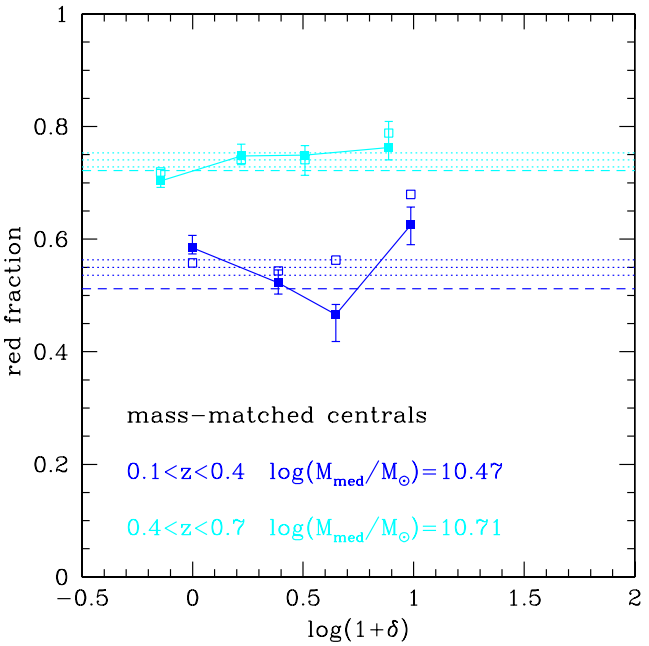

Figure 11. Red fractions of central galaxies as a function of overdensity. Symbols correspond to the red fraction measured at the median stellar mass $\log(M_{\rm med}/{\rm M}_\odot)$ of the mass-matched centrals in the four quartiles in overdensity. The error bars encompass the 16–84 per cent interval in the purity corrected red fractions of centrals from 20 realizations of the mass matching. The results are plotted at the median overdensity in each bin, where the empty and solid symbols correspond to the purity uncorrected and corrected quantities, respectively. The dotted lines mark the mean and the $\pm1\sigma$ interval of the four $f_{r,\rm cen}$ values. The dashed lines correspond to the red fraction from the best-fitting model (Table 2) at the median mass of centrals when assuming that only the mass quenching operates. The blue and cyan colours correspond to the results in $0.1 < z < 0.4$ and $0.4 < z < 0.7$, respectively.

to derive the red fractions of satellites, which are needed for the purity correction for the centrals, is driven by the small number of satellite galaxies in the regions of lowest overdensity.

We take the median in the distribution of purity-corrected red fractions of centrals from the 20 mass-matched samples to be our final result, and the 16–84 per cent interval in the same distribution as the $\pm1\sigma$ error interval. The obtained red fractions and the errors on the purity-corrected measurements are shown in Fig. 11.

We then repeat the mass-matching process for the sample of satellite galaxies in the equivalent way as for the centrals, defining the reference sample and the overdensity quartiles using the mass-complete sample of *satellites* in the two redshift bins. For the moment, we measure only the purity-uncorrected red fractions of satellites, as there are only a handfull of centrals of similar mass at the highest overdensities that are occupied by satellites. Similar to the centrals, we take for $\tilde{f}_{r,\rm sat}$ the median of red fractions from 20 mass-matched samples of satellites and take the 16–84 per cent interval in this distribution to be the $\pm1\sigma$ error. This is shown in Fig. 12. For reference, the weighted cumulative distribution functions (wCDFs) of stellar mass of the mass-matched samples of satellite galaxies are shown in Appendix B in Fig. B2.

We analyse now the colour–density relations for centrals and satellites that were obtained, shown in Figs 11 and 12, respectively. Even though the low-redshift measurements of the red fraction of centrals $f_{r,\rm cen}$ are quite noisy, there is little evidence for a strong trend with the overdensity in any redshift bin. To check whether

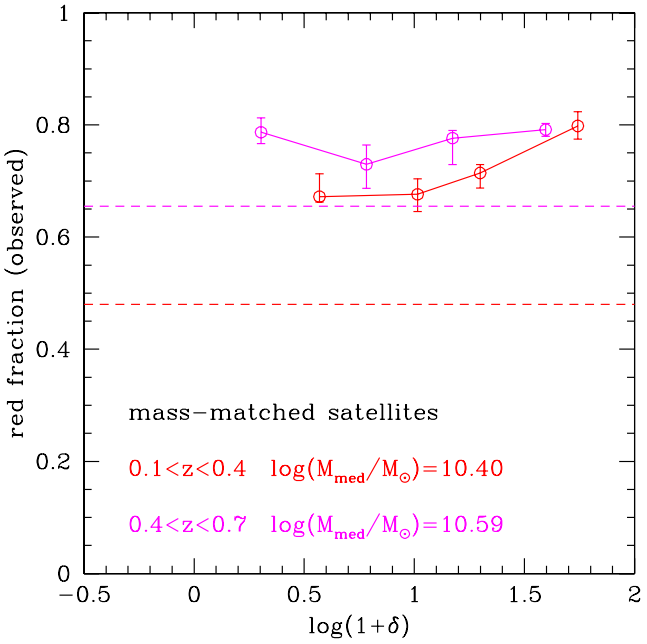

Figure 12. Red fractions of satellite galaxies as a function of overdensity. Symbols correspond to the red fractions measured at the median stellar mass $\log(M_{\rm med}/{\rm M}_\odot)$ of the mass-matched satellites in the four quartiles in overdensity. The error bars encompass the 16–84 per cent interval in the red fractions of satellites from 20 realizations of the mass matching. The results are uncorrected for purity, plotted at the median overdensity in each bin. The dashed lines correspond to the red fraction from the best-fitting model (Table 2) at the median mass of satellites when assuming that only the mass quenching operates. The red and magenta colours correspond to the results in $0.1 < z < 0.4$ and $0.4 < z < 0.7$, respectively.

environmental quenching is indeed negligible for centrals, as would be expected from the formalism of Peng et al. (2012), we calculate the red fraction of centrals that would be predicted from mass quenching alone, i.e. as given by equation (3) with the best-fitting parameters for $\epsilon_{\rm m}$ from Table 2 and $\epsilon_\rho = 0$. The expected red fractions, calculated at the median mass of central galaxies in the mass-matched samples, are 0.51 and 0.72 in the lower and higher redshift bins, respectively. These are plotted as the horizontal dashed lines in Fig. 11. The average $f_{r,\,\rm cen}$ values and their error intervals are calculated to be 0.55 ± 0.01 and 0.74 ± 0.01 in the equivalent redshift bins, and these are plotted as the dotted lines in Fig. 11. The $\epsilon_{\rm m}$-predicted red fractions differ by only a few per cent from the corrected red fraction of central galaxies derived from the data, leading us to conclude that the build-up of the red central galaxies is almost entirely due to the mass-quenching process. Any residual environmental quenching is increasing the red fraction of centrals by at most a few per cent (i.e. 2–4 per cent).

In contrast, the red fraction of satellites (Fig. 12) shows a rather clear dependence on overdensity in $0.1 < z < 0.4$, with $\tilde{f}_{r,\rm sat}$ increasing (by more than 10 per cent) with the increasing overdensity. In the $0.4 < z < 0.7$ range, the red fraction of satellites does not show a clear trend with overdensity. The red fractions of galaxies with $\log(M_*/{\rm M}_\odot) = 10.4$ and $\log(M_*/{\rm M}_\odot) = 10.59$, the median stellar masses of galaxies in the mass-matched samples of satellites in the lower and higher redshift bins, respectively, that would be expected to be produced by the mass-quenching process are 0.48 and 0.66. These are plotted as the dashed lines in Fig. 12 and are consistently lower than the observed red fractions of satellites. Environmental quenching has increased the red fraction of satellites by, on average, 23 per cent and 13 per cent, in the lower and higher redshift bins, respectively. Even though the conclusions which we presented so far for satellites are based on the impure quantities, due to the small number of equally massive centrals at the highest overdensity bins, this is of lesser concern than in the case of centrals, as the purity of satellites shows less change with overdensity, and is at 70–80 per cent even well below $\log(1+\delta) = 1$.

4.3 Satellite quenching

In the previous section, we have explored the dependence of the red fractions of centrals and satellites on the overdensity for galaxies with particular mass distributions. The results for centrals and satellites were obtained for different ranges of overdensity, since the reference samples of centrals cover a lower range in overdensity than that of the satellites. As a result, we could not correct the measured red fractions of satellites for impurity. It should be noted that the mass distribution of centrals is also systematically shifted to higher stellar masses compared with that of the satellites, and so the red fractions cannot be immediately compared since the different masses will have different red fractions from mass quenching.

We now analyse the environmental dependence of the *excess* in the red fraction of satellites with respect to the centrals. We create new samples of mass-matched centrals by matching their stellar masses (in the same four quartiles of overdensity, as defined by the centrals) to the reference mass distribution of the *satellite* galaxies in a given redshift bin. We follow the same matching procedure and the same estimation of red fractions and associated uncertainties as were described in Section 4.2. The resulting $f_{r,\,\rm cen}$ in the four overdensity quartiles are shown as solid squares in Fig. 13 in the upper and lower panels for the intervals $0.1 < z < 0.4$ and $0.4 < z < 0.7$, respectively. It should be noted that the values obtained are somewhat lower than when the masses are matched to the centrals (i.e. as in Fig. 11), because of the systematically lower stellar masses of the satellites. It is however reassuring that, as already shown previously, the red fractions of centrals do not show any strong trend with the overdensity, i.e. that we are not introducing some artificial colour–density trend by adopting a satellite mass distribution for the central galaxies. As before, the average red fractions of centrals (estimated to be 0.53 and 0.64 in the lower and upper redshift bins, respectively, and marked as the dashed lines in Fig. 13) are very close to the red fractions expected from purely mass quenching at the median stellar mass of satellites in the reference sample (estimated to be 0.48 and 0.66 in the lower and higher redshift bin, respectively).

Although the samples of centrals and satellites are now matched in mass, this still does not alleviate the fact that the red fractions of centrals and satellites are measured in systematically shifted ranges of overdensity. We deal with this by extrapolating a constant $f_{r,\,\rm cen}$ to the highest overdensities that are probed by the satellites, by taking the average value of $f_{r,\,\rm cen}$ that is measured for the centrals (the dashed lines in Fig. 13). The other possibility would have been to simply adopt the value expected from $\epsilon_{\rm m}$, but we prefer to use the measured values from the data whenever possible. Using this adopted $f_{r,\,\rm cen}$ for the whole range of overdensities, we can now also finally calculate the purity corrected $f_{r,\,\rm sat}$, which we did not do in Section 4.2, using equations (8) and (9). This is shown, for the two redshift bins, as the solid circles in Fig. 13.

The red fractions of satellites are, as expected, systematically above the red fractions of centrals up to $z = 0.7$ at all overdensities, due to the additional quenching process operating on the satellites. The excess of red satellites with respect to the centrals at a given

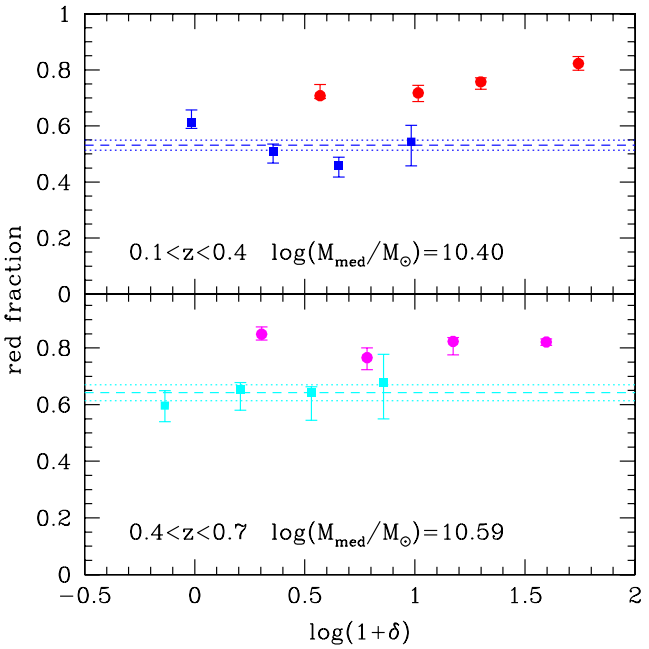

Figure 13. Red fractions of centrals (squares) and satellites (circles) that are mass-matched to the same distribution as a function of overdensity. Only the purity-corrected quantities are shown, measured at the median stellar mass $\log(M_{\rm med}/{\rm M}_\odot)$ in $0.1 < z < 0.4$ and $0.4 < z < 0.7$ in the top and bottom panels, respectively. The results are plotted at the median overdensity in the bins of overdensity quartiles. The respective errors encompass the 16–84 per cent interval of the purity-corrected red fractions of centrals or satellites in the 20 realizations of the mass matching. The dashed and dotted lines correspond to the average and $\pm1\sigma$ values of $f_{r,\,\rm cen}$.

overdensity δ and mass M_* is quantified by satellite quenching efficiency $\epsilon_{\rm sat}(\delta, M_*)$ defined as

$$\epsilon_{\rm sat}(\delta, M_*) = \frac{f_{r,{\rm sat}}(\delta, M_*) - f_{r,{\rm cen}}(M_*)}{f_{b,{\rm cen}}(M_*)}, \qquad (10)$$

where $f_{\rm b,cen}(M_*)$ is the blue fraction of centrals (Peng et al. 2012). The defined $\epsilon_{\rm sat}(\delta, M_*)$ quantity can then be interpreted as the excess fraction of satellite galaxies (in a given environment δ) which are environmentally quenched during the accretion process with respect to the population of star-forming centrals of the same stellar mass.

It can be argued (e.g. van den Bosch et al. 2008; Wetzel et al. 2013) that one should use, in equation (10), the $f_{r,{\rm cen}}(M_*)$ of the centrals at the (earlier) epoch at which the satellites first entered the halo. We digress for a moment to address this point, even though we will then argue that it is of no significance, because $f_{r,{\rm cen}}(M_*)$ actually changes little with redshift (see fig. 3 in Knobel et al. 2013). The choice of which $f_{r,{\rm cen}}(M_*)$ to use in equation (10) depends on what is assumed for the mass-quenching process. If mass quenching for some reason does not operate (at all) for satellites, then one should indeed use the $f_{r,{\rm cen}}$ at the earlier epoch (and at the slightly reduced stellar mass at which the satellite entered the halo). Alternatively, if mass quenching operates in exactly the same way for centrals and for satellites, even if mass quenching changes with time, then one should use the $f_{r,{\rm cen}}$ at the epoch of observation, simply because some of the satellites will have been mass quenched since they became satellites. We cannot be sure which scenario holds, although Peng et al. (2012) argued that the mass quenching should operate identically for satellites and centrals because star-forming centrals and star-forming satellites exhibit the same characteristic Schechter M*. However, regardless of these points, we would argue that in practice $f_{r,{\rm cen}}(M_*)$ changes little with redshift over the redshifts of interest (c.f. Wetzel et al. 2013). This is also evidenced by the constancy of $\epsilon_{\rm m}(M_*)$ over $0 < z < 0.7$ shown in Fig. 7.

We proceed with measuring $\epsilon_{\rm sat}(\delta, M_*)$ from the zCOSMOS data using the red fractions of centrals and satellites computed (at the same epoch) in the mass-matched samples. The $\epsilon_{\rm sat}(\delta, M_*)$ values, as computed in the four quartiles of satellite overdensity, are shown in Fig. 14 in green, using the solid and open symbols for the purity-corrected and -uncorrected quantities, respectively. The errors are shown only for the purity-corrected values and they are estimated by the propagation of errors on the individual fractions, using the symmetric $0.5(f_{r,{\rm cen}}(84\,{\rm per\,cent}) - f_{r,{\rm cen}}(16\,{\rm per\,cent}))$ and $0.5(f_{r,{\rm sat}}(84\,{\rm per\,cent}) - f_{r,{\rm sat}}(16\,{\rm per\,cent}))$ errors for the propagation. It should be noted that the $\epsilon_{\rm sat}(\delta, M_*)$ efficiencies measured above are obtained for a range of overdensities, especially for the lowest and highest quartiles. This will tend to smooth the measured $\epsilon_{\rm sat}(\delta, M_*)$ values in the extreme parts of the overdensity distribution.

As an independent estimate, we also measure $\epsilon_{\rm sat}(\delta, M_*)$ within the narrower range of overdensity where both populations exist in significant numbers. We calculate the red fractions in bins of overdensity that contain at least 20 centrals and 20 satellites and, as before, match the mass distribution of centrals to that of the satellites in a given overdensity bin following the procedure described in Section 4.2. The resulting $\epsilon_{\rm sat}(\delta, M_*)$ values are shown in red in Fig. 14, using the open and filled symbols for the purity-uncorrected and -corrected quantities. The median stellar masses in the overdensity bins, going from the lower to the higher δ are $\log(M_*/{\rm M}_\odot) =$ 10.24, 10.32 and 10.38 in $0.1 < z < 0.4$, and $\log(M_*/{\rm M}_\odot) =$ 10.49, 10.52 and 10.60 in $0.4 < z < 0.7$. The error interval corresponds to the 16–84 per cent range in the distribution of the $\epsilon_{\rm sat}(\delta, M_*)$ values obtained from the 50 mass-matched samples of centrals.

Leaving aside the differences in the stellar mass (which we will address later), we find that the differently measured $\epsilon_{\rm sat}(\delta, M_*)$ all paint a consistent picture on the dependence of satellite quenching efficiency on overdensity. The $\epsilon_{\rm sat}(\delta, M_*)$ measurements at the lower redshift show the satellite quenching efficiency increasing with the overdensity. We also show the value of $\epsilon_{\rm sat}(\delta)$ at $z \sim 0$ from the group analysis of Peng et al. (2012, orange lines in Fig. 14). We conclude that there is little evidence for any evolution in $\epsilon_{\rm sat}(\delta)$.

In the higher redshift bin, the $\epsilon_{\rm sat}(\delta, M_*)$ that is estimated in the two ways at the lowest overdensities are both just outside their respective 1σ error intervals. Considering the other points and their uncertainties our data do not, by themselves, show much evidence for a strong environmental dependence of $\epsilon_{\rm sat}(\delta, M_*)$. However, considering the larger errors on the $\epsilon_{\rm sat}(\delta, M_*)$ measurements and the shift to the lower $\log(1 + \delta)$ values in $0.4 < z < 0.7$, our higher redshift data also do not provide compelling evidence for any change of $\epsilon_{\rm sat}(\delta, M_*)$ with redshift between $z \sim 0$ and $z \sim 0.7$.

Turning back to the broader picture, in the case when the quenched fraction of centrals is produced solely through the mass-quenching process $\epsilon_{\rm m}$ (as strongly supported by the red fractions of zCOSMOS centrals, Fig. 11), then the ϵ_ρ of the overall population should be due to environmental quenching of the satellite population alone. In that case, $\epsilon_{\rm sat}(\delta, M_*)$ will be related to the environmental quenching through the fraction of satellites as $\epsilon_\rho(\delta)/f_{\rm sat}(\delta, M_*)$.

We can check this using $f_{\rm sat}(\delta, M_*)$ at the median stellar mass of satellites in the reference overdensity bin (i.e. $\log(M_*/{\rm M}_\odot)$ =10.40 and 10.59 in the two redshift bins), and at the lowest median stellar mass of satellites in the narrower overdensity bins (i.e. $\log(M_*/{\rm M}_\odot)$ =10.24 and 10.49 in the two redshift bins). These satellite fractions are calculated in $\log(M_*/{\rm M}_\odot) = 0.5$ bins,

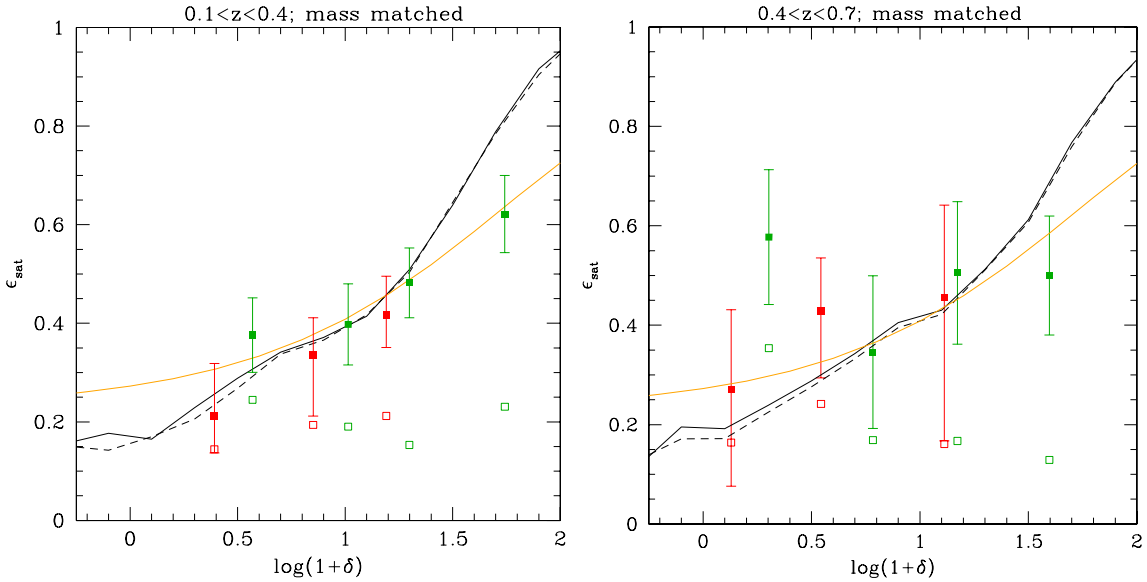

Figure 14. Satellite quenching efficiency $\epsilon_{\rm sat}$ as a function of overdensity in $0.1 < z < 0.4$ (left) and $0.4 < z < 0.7$ (right). The green symbols are the $\epsilon_{\rm sat}$ values measured from the data mass-matched in the quartiles of the satellite overdensity (with median mass $\log(M_*/{\rm M}_\odot)$ =10.40 and 10.59 in the lower and higher redshift bins, respectively). The red symbols are the $\epsilon_{\rm sat}$ values measured in the narrower bins of overdensity with at least 20 central and 20 satellite galaxies in each bin (with median masses $\log(M_*/{\rm M}_\odot) = 10.24$, 10.32 and 10.38, and 10.49, 10.52 and 10.60 in the lower and higher redshift bins, respectively). The solid and open symbols are for the purity-corrected and -uncorrected quantities, respectively. For clarity, the error bars are shown only for the former (see the text for more details). The black lines correspond to the model prediction $\epsilon_\rho(\delta)/f_{\rm sat}(\delta, M_*)$ valid in the case when the environmental quenching efficiency of centrals is negligible. The continuous and dashed lines are obtained for the fraction of satellites in the $\Delta\log(M_*/{\rm M}_\odot) = 0.5$ bin centred at $\log(M_*/{\rm M}_\odot) = 10.40$ (left) and 10.59 (right), and 10.24 (left) and 10.49 (right), respectively. For comparison, the orange line is the $z \sim 0$ $\epsilon_{\rm sat}(\delta)$ function averaged over all stellar masses from Peng et al. (2012).

centred at the quoted median mass. The resulting $\epsilon_\rho(\delta)/f_{\rm sat}(\delta, M_*)$ functions are shown in Fig. 14 as the black solid and dashed lines, respectively. They differ only slightly, reflecting the very weak dependence of $f_{\rm sat}(\delta, M_*)$ on mass.

The $\epsilon_{\rm sat}(\delta, M_*)$ measurements from the narrower overdensity bins show an excellent agreement with the expected $\epsilon_\rho(\delta)/f_{\rm sat}(\delta, M_*)$ values in both redshifts. The $\epsilon_{\rm sat}(\delta, M_*)$ measurements from the quartiles in the overdensity are also broadly consistent, and only the highest quartile point at the lower redshift bin and the lowest quartile point at the higher redshift bin are significantly discrepant. As we have already mentioned, these points cover the broadest ranges in overdensity and therefore must be rather smoothed. Taking this all together, still the agreement between the measured $\epsilon_{\rm sat}(\delta, M_*)$ points and the value of $\epsilon_\rho(\delta)/f_{\rm sat}(\delta, M_*)$ is rather striking.

Our detailed analysis strongly suggests that the satellite galaxies must be the dominant population of galaxies that is driving the overall environmental trends at least up to $z = 0.7$. The net effect in the overall population ϵ_ρ is the combination of two dependences on overdensity: the $\epsilon_{\rm sat}(\delta, M_*)$ and $f_{\rm sat}(\delta, M_*)$ functions. Furthermore, the effect of the environment on satellites, at least if environment is defined by our overdensity parameter, is consistent with being unchanged at $z = 0.7$ compared with $z \sim 0$.

It is clear that the constancies highlighted in this paper are unlikely to be exact. First, the functions $\epsilon_\rho(\delta)$ and $\epsilon_{\rm sat}(\delta, M_*)$ are simple representations of no doubt complex physical processes. Secondly, our chosen environment parameter, an overdensity δ, is observationally convenient but is unlikely to correspond *exactly* to a physically relevant parametrization of environment (we return to this point in the next section). Finally since $f_{\rm sat}$ is unlikely to be completely independent of stellar mass and of epoch, it is clear that it is not possible for both (or possibly either) ϵ_ρ and $\epsilon_{\rm sat}$ to be strictly independent of mass and time. It is also clear that, even with our very large sample, the statistical uncertainties become significant when the sample is split into centrals and satellites, into bins of overdensity and further selected via the mass-matching procedure. For all these reasons, our statements should be taken as 'approximations to reality' rather than as a statement of physical exactitude.

5 WHICH ENVIRONMENT MATTERS?

One of the difficulties when interpreting the observed correlation between galaxy environment and other properties is the choice of the definition of environment. The quantification of environment by the number density of galaxies within some apertures (fixed or adaptive) is the most commonly used environmental indicator based on the observational data, as it is rather straightforward to calculate (but see the discussion on the reconstruction process and various uncertainties in e.g. Kovač et al. 2010a). However, it is questionable what is the physical meaning of such defined environment.

In most theoretical studies, dark matter haloes are considered to be the key drivers of galaxy evolution, and their properties have been most commonly used as an environment indicator. The number density of galaxies and their halo masses are certainly correlated, but the dispersion of the halo masses at a measured density can be 1 dex or more (e.g. Haas, Schaye & Jeeson-Daniel 2012). In order to reconcile the two indicators and constrain the physical process responsible for the observed environmental differences in the galaxy population, one ideally needs to constrain both environment estimators on the same data set. Assignment of the observed galaxies to common haloes (i.e. the group finding process) and measuring the properties of the haloes is observationally not a straightforward task as it usually requires, for all except the richest structures, some calibration against mock catalogues or other theoretical distributions. The reconstructed groups and their derived properties will suffer

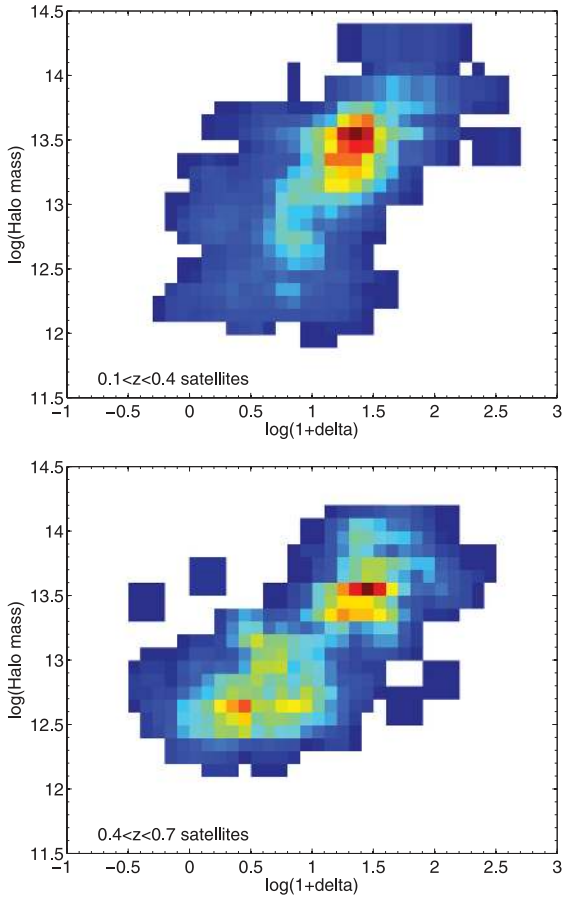

Figure 15. Relation between halo mass and overdensity for satellite galaxies in the mass-complete samples. The top and bottom panels are for $0.1 < z < 0.4$ and $0.4 < z < 0.7$, respectively. The colour coding corresponds to the number density of galaxies in a given bin (going from blue to red as the number density increases).

from uncertainties usually quantified by the purity and completeness, and particularly by the error on the estimated halo properties, which increases for groups with only a few members.

It has been pointed out previously that the environment indicator based on the nearest N neighbour counts, as used in this paper, has a dual nature with respect to the parent galaxy halo. For the richest structures with more than N tracer galaxies, the reconstructed δ is a measure of the density within the halo, while for less rich structures the δ will be a measure of the environment surrounding the halo (e.g. Weinmann et al. 2006; Haas et al. 2012; Muldrew et al. 2012; Peng et al. 2012; Skibba et al. 2013; Woo et al. 2013).

The virial radius of a halo is often considered to be a physically motivated scale up to which the environment plays a role, as dynamically galaxies within the virial radius cannot be much influenced by galaxies outside of it (Weinmann et al. 2006). The virial radius marks also a transition between smooth infall and virial motions, the latter providing support for the strong shock fronts and hot, thermalized gas (e.g. Dekel & Birnboim 2006). However, there is observational evidence that the environmental trends observed within the virial radius extend to the distance of a few virial radii (Balogh et al. 1999; Hansen et al. 2009; von der Linden et al. 2010; Lu et al. 2012). Part of this can be explained through the non-sphericity of haloes (e.g. Weinmann et al. 2006), or it can originate from galaxies already quenched within a group that falls into more massive structure (i.e. pre-processing; Berrier et al. 2009; Li, Yee & Ellingson 2009; McGee et al. 2009), satellite galaxies outside of the virial radius after the first pericentric passage caused by the highly eccentric orbits (i.e. overshooting; Benson 2005; Ludlow et al. 2009; Wetzel 2011) or the recently proposed interaction of galaxies with the hot gas in filaments (Bahé et al. 2012). In addition, from the theoretical point of view properties of dark matter haloes also depend on their environment through the so-called 'assembly bias' (Gao, Springel & White 2005; Gao & White 2006; Wechsler et al. 2006). All this complicates the identification of a key environment (or a key environmental scale) in the evolution of galaxies.

In the case of zCOSMOS satellites studied in this paper, the projected distance to the fifth nearest neighbour in the $M_B < -19.3 - z$ sample of tracer galaxies varies between 0.4–4.9 h^{-1}Mpc (mean 2.6 h^{-1}Mpc) and 0.35–5.0 h^{-1}Mpc (mean 2.71 h^{-1}Mpc) in $0.1 < z < 0.4$ and $0.4 < z < 0.7$, respectively. These values are much larger than the average virial radius of reconstructed zCOSMOS groups in the Henriques et al. (2012) mocks, which is 0.33 and 0.35 physical Mpc in the lower and higher redshift bin, respectively. Furthermore, the ± 1000 km s^{-1} interval over which we project galaxies in the radial dimension corresponds to 21.1, 23.4 and 24.2 h^{-1}Mpc at 0.1, 0.4 and 0.7, respectively. Even though at a first instance this interval seems large, it is similar to the line-of-sight length of a cylinder used for the Voronoi–Delaunay method for the group reconstruction in both the zCOSMOS (Knobel et al. 2009, 2012a) and the DEEP2 and AEGIS (Gerke et al. 2007, 2012), optimized to account for the peculiar velocities of group galaxies.

As described in Section 2.5, Knobel et al. (2012a) provide estimates for the halo masses for our zCOSMOS groups. This is based on calibration against mock catalogues, coupled with a study of the cross-correlation function of groups and galaxies (Knobel et al. 2012b). The relation between the halo mass and the adopted overdensity of the zCOSMOS satellites that is used in this work is shown in Fig. 15. There is a broad correlation between the two environment indicators: the satellites in the most massive haloes simultaneously reside in the most overdense (in projection) environments, and vice versa, though the correlation has a lot of scatter. In addition, one needs to keep in mind that the reconstructed halo masses have substantial uncertainties (Knobel et al. 2009, 2012a).

Are the observed trends with overdensity discussed above due to a primary correlation with halo mass? Fig. 16 shows the fraction of red satellite galaxies in the halo mass–overdensity plane for a $9.82 < \log(M_*/\mathrm{M}_\odot) < 10.32$ subset in $0.1 < z < 0.4$. It should be noted that we cannot correct the obtained fractions for the purities of central and satellite samples since we do not know (at this point) how these depend on halo mass. The red fraction does not show a stronger correlation with either of the two environmental indicators (black contours in Fig. 16). We reach the same conclusion also for the satellites of higher stellar mass at both redshift bins. Within our own data set, it is hard to distinguish whether the halo mass or the overdensity of the zCOSMOS satellite galaxies at $0.1 < z < 0.7$ has a more important role in building the red fraction of satellite galaxies.

The situation at low redshift is better: in SDSS, Peng et al. (2012) concluded that halo mass was a relatively minor component and that local overdensity was the dominant driver of the relation between the red fraction of satellites and their environment [similar conclusion was obtained also by Cibinel et al. 2013 using the local Zurich ENvironmental Study (ZENS) groups]. Woo et al. (2013) presented a more complex picture in which a halo mass dependence was present for only the highest density environments.

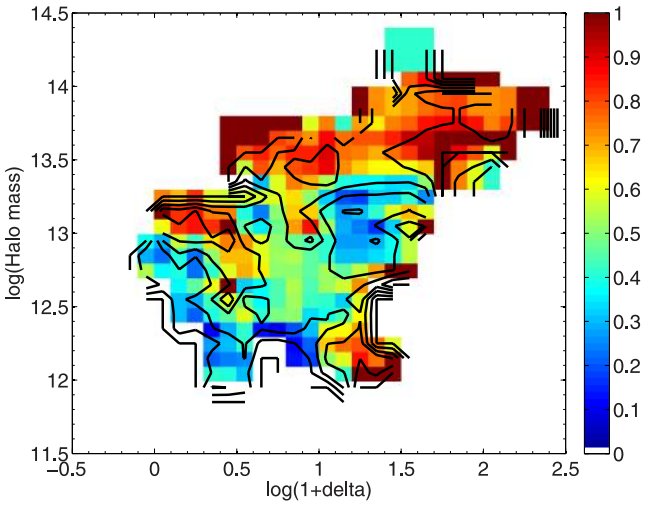

Figure 16. Red fraction of satellite galaxies in the halo mass–overdensity plane. Galaxies have stellar mass in the range $9.82 < \log(M_*/\mathrm{M}_\odot) < 10.32$ in $0.1 < z < 0.4$. The colour scale corresponds to the red fraction of satellites measured in a given halo mass–overdensity bin, as indicated by the bar on the right-hand side. The black contours follow the same colour scale and are separated by 0.2.

Peng et al. (2012) used the $9.5 < \log(M_*/\mathrm{M}_\odot) < 10.0$ subsample of satellites to reach the above conclusion. These are amongst the most populous satellites and they dominate the outskirts of the groups (see the white contours in the right-hand panel in fig. 10 in Woo et al. 2013), for which Woo et al. also concluded that the halo quenching is weakest, bringing these two works into agreement on the roles of halo mass and local overdensity in quenching of satellites. In addition, using also SDSS, Tinker, Wetzel & Conroy (2011) found that the increase in the quenched fraction of satellites at a given luminosity (or stellar mass) with the large-scale environment is due to variations of the halo mass with overdensity, i.e. that at a given large-scale overdensity and a luminosity bin, the fraction of quenched satellites increases with the halo mass. It is possible that for satellites the small-scale environment measured by the nearest neighbour technique (used by Peng et al. and Woo et al.) correlates stronger with halo mass than with the overdensity measured on the 10 h^{-1}Mpc scale (used by Tinker et al.), bringing all these results in agreement.

We also have too few centrals with measurable halo masses to meaningfully examine any residual dependence of the red fraction of centrals on halo mass, although noting that this could not be large because of the apparent independence of this quantity with local overdensity. In SDSS, there is some evidence that, at fixed stellar mass, central galaxies in higher mass haloes have a higher red fraction (Woo et al. 2013) but this can be understood in terms of the differential build-up of dark mass after a galaxy has ceased making stars (Peng et al. 2012). On the other hand, given that the properties of central galaxies in the relaxed and unrelaxed $z \sim 0$ ZENS groups do not change much, Carollo et al. (2013) concluded that the properties of central galaxies must be driven by stellar mass.

Woo et al. (2013) also explored the relations between the quenched fractions of galaxies and their stellar and halo mass and overdensity in $0.75 < z < 1$ using the AEGIS data. Due to the low number of satellites, they obtained results only for the central galaxies at these redshifts, finding that for the majority of centrals their quenched fraction correlates better with stellar than halo mass. Moreover, Woo et al. found no correlation between the halo mass and the overdensity for the central galaxies in the AEGIS sample. The quenched fraction of AEGIS centrals clearly increases with stellar mass (see also Cheung et al. 2012), in agreement with the zCOSMOS results in Knobel et al. (2013) and the ϵ_m-model for the red fraction of centrals presented in this paper. Importantly, the quenched fraction of the AEGIS centrals does not show any correlation with the local overdensity, echoing the results presented in this work.

6 CONCLUSIONS

In this paper, we have studied the origin of environmental effects in the star formation properties of galaxies at significant look-back times. Our analysis is based on the final zCOSMOS-bright data set, containing about 17 000 galaxies with reliable spectroscopic redshifts. These same galaxies, complemented by some information on those galaxies in the parent catalogue that do not have reliable spectroscopic redshift, are also used to reconstruct the overdensities based on a nearest neighbour algorithm, which we use as a primary environmental indicator in this paper. Separation of the galaxies into centrals and satellites is done using the group catalogue of Knobel et al. (2012a). Finally, we carefully considered, in deriving our results, the effects of incompleteness in stellar mass and the impurity of the central-satellite classification.

We first studied the colour–mass–density relation by measuring the red fraction of galaxies $f_\mathrm{red}(M_*, \delta)$ in bins of stellar mass and overdensity δ in two redshift bins, $0.1 < z < 0.4$ and $0.4 < z < 0.7$.

(1) As previously observed, the red fraction of galaxies increases with the environmental overdensity, for galaxies of a given stellar mass, and with mass at a given overdensity, out to $z = 0.7$, the highest redshift that we could examine.

(2) As in the local galaxy population (Baldry et al. 2006; Peng et al. 2010), such dependence of f_red on mass and environment can be approximated by the functional form $1 - f_\mathrm{red}(M_*, \delta) = (1 - \epsilon_\mathrm{m}(M_*))(1 - \epsilon_\rho(\delta))$ in which the dependence on mass and environment is separable. The measured f_red can be well represented by this function in both our redshift bins, always within 2σ and without systematic deviations in either mass or overdensity. Given the limited size of the current data set, we cannot exclude the existence of a cross term in both mass and environment, but this must be within the estimated statistical uncertainties. If they exist at all, such effects would represent a small addition to the picture, rather than changing the model completely.

(3) Following our previous paper, we interpret this separability as indication that two independent processes dominate the quenching of galaxies, mass quenching and environmental quenching. The parameters that describe these two processes, i.e. $\epsilon_\mathrm{m}(M_*)$ and $\epsilon_\rho(\delta)$ do not, within the uncertainties, change with redshift, and are consistent with their respective equivalents measured at $z \sim 0$ from SDSS (Peng et al. 2010). Lack of change in $\epsilon_\mathrm{m}(M_*)$ is expected from the observation of a constant value of M_* of star-forming galaxies, but the lack of change in $\epsilon_\rho(\delta)$ is less obviously required.
Using samples of centrals and satellites that are carefully matched in stellar mass, we investigated further the colour–density relation for the centrals and satellites separately.

(4) We find that the red fraction of centrals $f_{r,\,\mathrm{cen}}$ is primarily a function of mass and is almost independent of overdensity at both epochs studied. The red fraction of centrals is therefore consistent with being produced almost entirely by the mass-quenching process alone, with any environmental effects (as traced by the overdensity)

increasing the red fraction by at most a few per cent (less than 5 per cent).

(5) In contrast to this, the red fraction of satellite galaxies $f_{r,\,\mathrm{sat}}$ requires additional environmental quenching in order to explain the observed red fractions at a given stellar mass and overdensity. This is particularly obvious in $0.1 < z < 0.4$, where we find that $f_{r,\,\mathrm{sat}}$ clearly increases with the overdensity.

(6) The overall satellite fraction f_{sat} is a strong function of overdensity, increasing from practically zero at the lowest overdensities and reaching more than 0.9 at the highest overdensities. There is only a very weak dependence of f_{sat} on stellar mass. For satellites with $\log(M_*/\mathrm{M}_\odot) \sim 10.5$ (for which we are statistically complete at both redshifts) there is no evidence for a redshift evolution in the satellite fraction at a given overdensity.

(7) At the same stellar mass, the red fraction of satellites is higher than the red fraction of centrals over the whole range of overdensities. This excess of red satellites with respect to the centrals at a given overdensity δ and mass M_*, normalized by the blue fraction of centrals at the same mass, is used to measure the satellite quenching efficiency, $\epsilon_{\mathrm{sat}}(\delta, M_*)$. The satellite quenching efficiency at $0.1 < z < 0.4$ increases with overdensity and is noticeably consistent with the equivalent $z \sim 0$ measurements in the SDSS (Peng et al. 2012). In $0.4 < z < 0.7$, our $\epsilon_{\mathrm{sat}}(\delta, M_*)$ measurements do not show much evidence for a strong environmental dependence, but, taking into account the statistical uncertainties as well as the shift to the lower overdensities in the higher redshift bin, the overall conclusion is that $\epsilon_{\mathrm{sat}}(\delta, M_*)$ stays unchanged from $z \sim 0$ to $z \sim 0.7$.

(8) Our results demonstrate an overall agreement between the measured $\epsilon_{\mathrm{sat}}(\delta, M_*)$ points and the value of $\epsilon_\rho(\delta)/f_{\mathrm{sat}}(\delta, M_*)$, where the equality between the last two expressions will hold when the environmental quenching in the overall population is entirely produced through the satellite quenching process.

The main conclusion from our analysis is that satellite galaxies are the main drivers of the observed trends in the quenched fraction with overdensity at least up to $z = 0.7$. The relative role of environment, quantified by either ϵ_ρ or ϵ_{sat}, does not change significantly with redshift, and is consistent with the $z \sim 0$ measurements. However, for the satellite population, the dependence of the red fraction on the environmental overdensity is very similar to its dependence on the halo mass, making these two environment indicators statistically equivalent within our data set of satellites.

Although based on a straight colour-division of the population, all of the above statements remain valid when using the $(\mathrm{NUV} - r) - (r - J)$ two-colour plane to define the quenched fraction.

Finally, given the limited size of our sample when split in bins of redshift, mass, overdensity and populations of centrals and satellites, the above relations should be regarded as approximations to a complex reality, rather than as mathematical identities.

ACKNOWLEDGEMENTS

This work is based on observations obtained at the European Southern Observatory (ESO) Very Large Telescope (VLT), Paranal, Chile, as part of the Large Programme 175.A-0839 (the zCOSMOS Spectroscopic Redshift Survey). This research was supported by the Swiss National Science Foundation. The Millennium Simulation data bases used in this paper and the web application providing online access to them were constructed as part of the activities of the German Astrophysical Virtual Observatory.

REFERENCES

Abadi M. G., Moore B., Bower R. G., 1999, MNRAS, 308, 947
Bahé Y. M., McCarthy I. G., Crain R. A., Theuns T., 2012, MNRAS, 424, 1179
Baldry I. K., Balogh M. L., Bower R. G., Glazebrook K., Nichol R. C., Bamford S. P., Budavari T., 2006, MNRAS, 373, 469
Balogh M. L., Morris S. L., 2000, MNRAS, 318, 703
Balogh M. L., Morris S. L., Yee H. K. C., Carlberg R. G., Ellingson E., 1999, ApJ, 527, 54
Balogh M. L., Navarro J. F., Morris S. L., 2000, ApJ, 540, 113
Balogh M. et al., 2004, MNRAS, 348, 1355
Bardelli S. et al., 2010, A&A, 511, A1
Benson A. J., 2005, MNRAS, 358, 551
Berrier J. C., Stewart K. R., Bullock J. S., Purcell C. W., Barton E. J., Wechsler R. H., 2009, ApJ, 690, 1292
Blanton M. R., Eisenstein D., Hogg D. W., Schlegel D. J., Brinkmann J., 2005, ApJ, 629, 143
Bolzonella M. et al., 2010, A&A, 524, A76
Boselli A., Gavazzi G., 2006, PASP, 118, 517
Bruzual G., Charlot S., 2003, MNRAS, 344, 1000
Bundy K. et al., 2010, ApJ, 719, 1969
Calzetti D., Armus L., Bohlin R. C., Kinney A. L., Koornneef J., Storchi-Bergmann T., 2000, ApJ, 533, 682
Capak P. et al., 2007, ApJS, 172, 99
Caputi K. I. et al., 2009, ApJ, 691, 91
Carollo C. M. et al., 2013, ApJ, 776, 71
Chabrier G., 2003, PASP, 115, 763
Cheung E. et al., 2012, ApJ, 760, 131
Chuter R. W. et al., 2011, MNRAS, 413, 1678
Cibinel A. et al., 2013, ApJ, 777, 116
Cooper M. C. et al., 2007, MNRAS, 376, 1445
Cooper M. C. et al., 2010, MNRAS, 409, 337
Cucciati O. et al., 2006, A&A, 458, 39
Cucciati O. et al., 2010, A&A, 524, A2
Davis M., Geller M. J., 1976, ApJ, 208, 13
Dekel A., Birnboim Y., 2006, MNRAS, 368, 2
Dressler A., 1980, ApJ, 236, 351
Farouki R., Shapiro S. L., 1981, ApJ, 243, 32
Feldmann R. et al., 2006, MNRAS, 372, 565
Feldmann R., Carollo C. M., Mayer L., 2011, ApJ, 736, 88
Gao L., White S. D. M., 2006, MNRAS, 373, 65
Gao L., Springel V., White S. D. M., 2005, MNRAS, 363, L66
Gerke B. F. et al., 2007, MNRAS, 376, 1425
Gerke B. F. et al., 2012, ApJ, 751, 50
Gunn J. E., Gott J. R. I., 1972, ApJ, 176, 1
Guo Q. et al., 2011, MNRAS, 413, 101
Haas M. R., Schaye J., Jeeson-Daniel A., 2012, MNRAS, 419, 2133
Hansen S. M., Sheldon E. S., Wechsler R. H., Koester B. P., 2009, ApJ, 699, 1333
Henriques B. M. B., White S. D. M., Lemson G., Thomas P. A., Guo Q., Marleau G.-D., Overzier R. A., 2012, MNRAS, 421, 2904
Hogg D. W. et al., 2004, ApJ, 601, L29
Hubble E., 1939, Publ. Am. Astron. Soc., 9, 249
Ilbert O. et al., 2010, ApJ, 709, 644
Ilbert O. et al., 2013, A&A, 556, A55
Iovino A. et al., 2010, A&A, 509, A40
Jian H.-Y., Lin L., Chiueh T., 2012, ApJ, 754, 26
Kampczyk P. et al., 2013, ApJ, 762, 43
Kauffmann G. et al., 2003, MNRAS, 341, 54
Kauffmann G., White S. D. M., Heckman T. M., Ménard B., Brinchmann J., Charlot S., Tremonti C., Brinkmann J., 2004, MNRAS, 353, 713
Kennicutt R. C., Jr, 1998, ARA&A, 36, 189
Kitzbichler M. G., White S. D. M., 2007, MNRAS, 376, 2
Knobel C. et al., 2009, ApJ, 697, 1842
Knobel C. et al., 2012a, ApJ, 753, 121
Knobel C. et al., 2012b, ApJ, 755, 48
Knobel C. et al., 2013, ApJ, 769, 24

Kovač K. et al., 2010a, ApJ, 708, 505
Kovač K. et al., 2010b, ApJ, 718, 86
Larson R. B., Tinsley B. M., Caldwell C. N., 1980, ApJ, 237, 692
Le Fèvre O. et al., 2003, in Iye M., Moorwood A. F. M., eds, SPIE Conf. Ser. Vol. 4841, Instrument Design and Performance for Optical/Infrared Ground-based Telescopes. SPIE, Bellingham, p. 1670
Le Floc'h E. et al., 2009, ApJ, 703, 222
Li I. H., Yee H. K. C., Ellingson E., 2009, ApJ, 698, 83
Lilly S. J. et al., 2007, ApJS, 172, 70
Lilly S. J. et al., 2009, ApJS, 184, 218
Lilly S. J., Peng Y., Carollo M., Renzini A., 2013, in Thomas D., Pasquali A., Ferreras I., eds, Proc. IAU Symp. Vol. 295, The Intriguing Life of Massive Galaxies. Cambridge Univ. Press., Cambridge, p. 141
Lu T., Gilbank D. G., McGee S. L., Balogh M. L., Gallagher S., 2012, MNRAS, 420, 126
Ludlow A. D., Navarro J. F., Springel V., Jenkins A., Frenk C. S., Helmi A., 2009, ApJ, 692, 931
McCarthy I. G., Frenk C. S., Font A. S., Lacey C. G., Bower R. G., Mitchell N. L., Balogh M. L., Theuns T., 2008, MNRAS, 383, 593
McDonald M., Veilleux S., Mushotzky R., 2011, ApJ, 731, 33
McGee S. L., Balogh M. L., Bower R. G., Font A. S., McCarthy I. G., 2009, MNRAS, 400, 937
Moore B., Lake G., Katz N., 1998, ApJ, 495, 139
Moresco M. et al., 2013, A&A, 558, A61
Muldrew S. I. et al., 2012, MNRAS, 419, 2670
Oemler A., Jr, 1974, ApJ, 194, 1
Oesch P. A. et al., 2010, ApJ, 714, L47
Peng Y.-j. et al., 2010, ApJ, 721, 193
Peng Y.-j., Lilly S. J., Renzini A., Carollo M., 2012, ApJ, 757, 4
Quadri R. F., Williams R. J., Franx M., Hildebrandt H., 2012, ApJ, 744, 88
Quilis V., Moore B., Bower R., 2000, Science, 288, 1617
Raichoor A., Andreon S., 2012, A&A, 543, A19
Rasmussen J., Ponman T. J., Mulchaey J. S., 2006, MNRAS, 370, 453
Read J. I., Wilkinson M. I., Evans N. W., Gilmore G., Kleyna J. T., 2006, MNRAS, 366, 429
Sanders D. B. et al., 2007, ApJS, 172, 86
Scoville N. et al., 2007a, ApJS, 172, 38
Scoville N. et al., 2007b, ApJS, 172, 150
Scoville N. et al., 2013, ApJS, 206, 3
Silverman J. D. et al., 2009, ApJ, 695, 171
Skibba R. A., Sheth R. K., Croton D. J., Muldrew S. I., Abbas U., Pearce F. R., Shattow G. M., 2013, MNRAS, 429, 458
Tasca L. A. M. et al., 2009, A&A, 503, 379
Tinker J., Wetzel A., Conroy C., 2011, preprint (arXiv:1107.5046)
Tinker J. L., Leauthaud A., Bundy K., George M. R., Behroozi P., Massey R., Rhodes J., Wechsler R. H., 2013, ApJ, 778, 93
van den Bosch F. C., Aquino D., Yang X., Mo H. J., Pasquali A., McIntosh D. H., Weinmann S. M., Kang X., 2008, MNRAS, 387, 79
van der Burg R. F. J. et al., 2013, A&A, 557, A15
Vergani D. et al., 2010, A&A, 509, A42
von der Linden A., Wild V., Kauffmann G., White S. D. M., Weinmann S., 2010, MNRAS, 404, 1231
Wechsler R. H., Zentner A. R., Bullock J. S., Kravtsov A. V., Allgood B., 2006, ApJ, 652, 71
Weinmann S. M., van den Bosch F. C., Yang X., Mo H. J., 2006, MNRAS, 366, 2
Weinmann S. M., Kauffmann G., van den Bosch F. C., Pasquali A., McIntosh D. H., Mo H., Yang X., Guo Y., 2009, MNRAS, 394, 1213
Wetzel A. R., 2011, MNRAS, 412, 49
Wetzel A. R., Tinker J. L., Conroy C., 2012, MNRAS, 424, 232
Wetzel A. R., Tinker J. L., Conroy C., van den Bosch F. C., 2013, MNRAS, 432, 336
White D. A., Jones C., Forman W., 1997, MNRAS, 292, 419
Williams R. J., Quadri R. F., Franx M., van Dokkum P., Labbé I., 2009, ApJ, 691, 1879
Woo J. et al., 2013, MNRAS, 428, 3306
Wuyts S. et al., 2011, ApJ, 738, 106
York D. G. et al., 2000, AJ, 120, 1579

APPENDIX A: DIFFERENCE BETWEEN THE MODELLED AND MEASURED RED FRACTIONS OF ZCOSMOS GALAXIES

We showed, in Fig. 5 (Section 3.2), the red fraction of galaxies both expected from the model and measured from the zCOSMOS data in the $\log(1+\delta) - \log(M_*/\mathrm{M}_\odot)$ plane. Here, we show in Fig. A1 the differences between the two, normalized by the adopted 1σ uncertainties at each $\Delta\log(1+\delta) = \Delta\log(M_*/\mathrm{M}_\odot) = 0.3$ bin. We show the results only for the range of stellar mass and overdensity which were used to fit equation (2). The key conclusion is that there are no systematic trends in the normalized differences between the model and the data across the overdensity–mass range probed by our data.

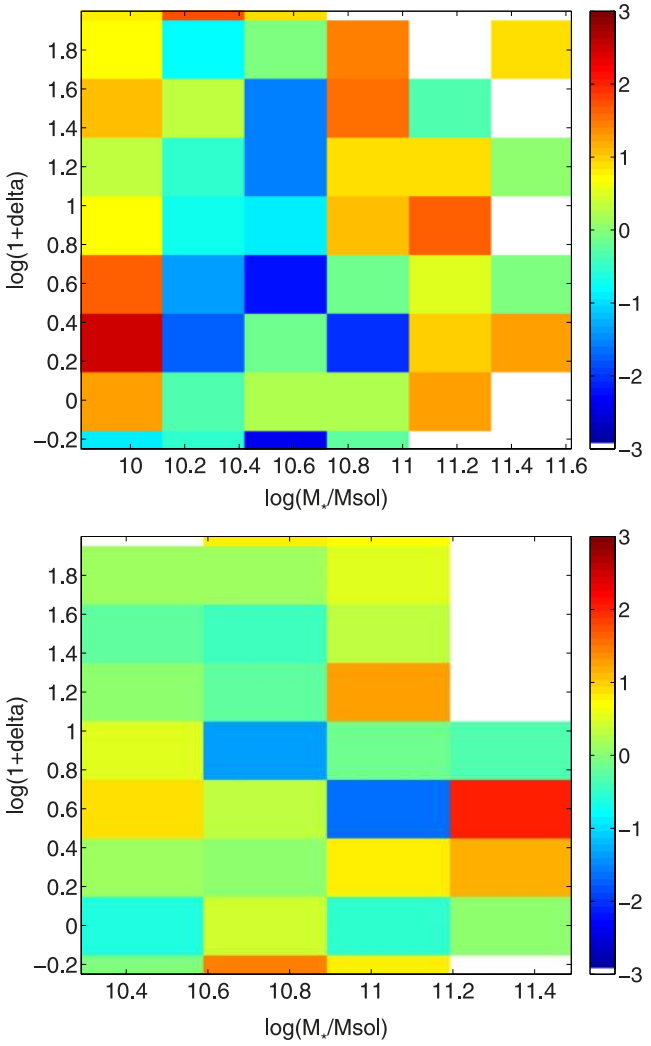

Figure A1. Difference between the modelled and measured red fraction normalized by the adopted error. The obtained values are colour-coded according to the bar shown on the right-hand side. The bins without data are artificially set to have the low negative values (white fields). The top and bottom panels are for the two redshift bins: $0.1 < z < 0.4$ and $0.4 < z < 0.7$, respectively.

APPENDIX B: MASS DISTRIBUTION OF GALAXIES IN THE MATCHED SAMPLES

We described in Section 4.2, the procedure to match in stellar mass different samples of galaxies residing in different bins of overdensities. In this appendix, we provide some additional, more quantitative details of the matching procedure and show the resulting weighted stellar mass distributions of the matched samples of centrals and satellites.

The mass-matching process consists of randomly choosing a galaxy in each of the overdensity quartiles with stellar mass close to a galaxy in the reference sample, for each galaxy in the reference sample. The nominal absolute difference in the $\log(M_*/\mathrm{M}_\odot)$ values which we use to pair galaxies is 0.01, though this difference could be enlarged if no suitable galaxy is found. The created samples of central or satellite galaxies in a given quartile of overdensity are then compared to their respective reference sample by comparing their wCDFs of stellar mass. We consider the wCDFs of stellar masses in the two samples to be matched if the absolute normalized difference between the two wCDFs at any percentile is less than 0.01 (see Kauffmann et al. 2004 for a similar approach in comparing distributions). We use for normalization the range in mass corresponding to the 1–99 per cent interval of the wCDF in the reference sample. In practice, we measure the differences at 99 points equally distributed between 1 and 99 per cent of the wCDF in the reference sample. If the distributions are not matched according to our criteria, we discard the matched sample and redo the matching. We repeat the process until we have produced 20 samples matched according to the outlined criteria in each overdensity and redshift bin. The resulting wCDFs of stellar mass of the mass-matched central and satellite galaxies are shown in Figs B1 and B2, respectively.

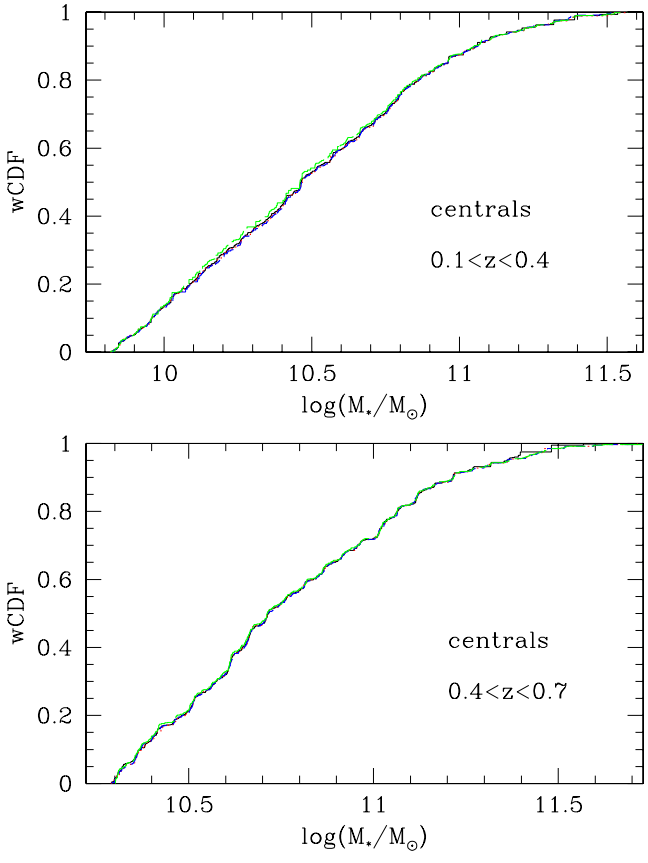

Figure B1. Weighted cumulative distribution functions of stellar mass in the samples of mass-matched centrals. The top and bottom panels are for $0.1 < z < 0.4$ and $0.4 < z < 0.7$, respectively. Different curves are constructed from the samples of centrals in the four quartiles of overdensity distribution defined by the central galaxies in a given redshift bin.

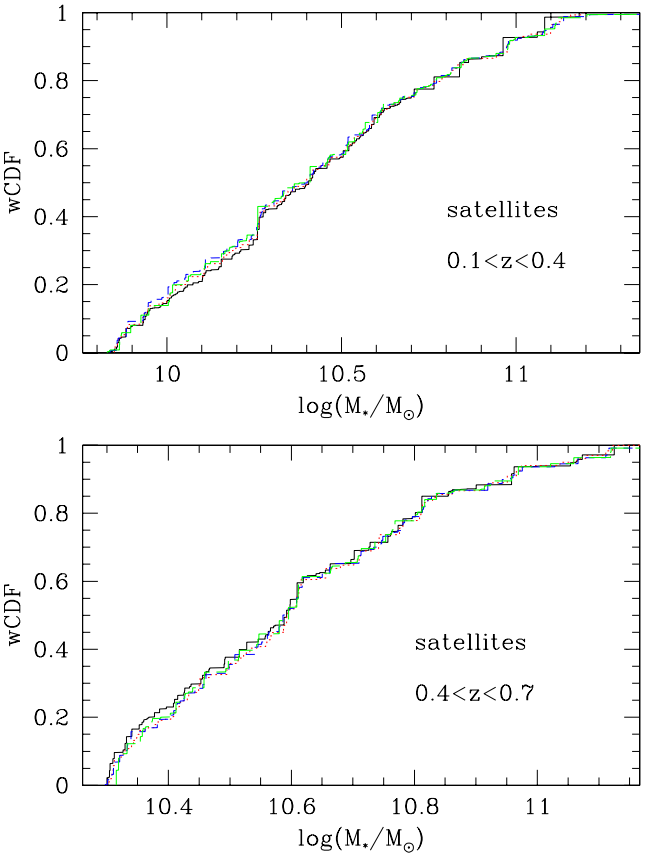

Figure B2. Weighted cumulative distribution functions of stellar mass in the samples of mass-matched satellites. The top and bottom panels are for $0.1 < z < 0.4$ and $0.4 < z < 0.7$, respectively. Different curves are constructed from the samples of satellites in the four quartiles of overdensity distribution defined by the satellite galaxies in a given redshift bin.

APPENDIX C: RESULTS OBTAINED USING COLOUR–COLOUR SELECTION TO DEFINE QUENCHED GALAXIES

The results presented in this paper are obtained when using the SED-estimated rest-frame $U - B$ colour to identify red galaxies, which we use as a proxy for the quenched population. We discussed the influence of separating galaxies into star-forming and quenched populations based on their SFR in Section 2.2.3, concluding that the results from our analysis should qualitatively remain the same when using either the colour or SFR to define the quenched population, as the difference in the fractions of quenched galaxies selected in the two different ways is almost independent of stellar mass. We focused on the SFR-based separation of galaxies in such comparison, as for a significant fraction of galaxies (about 45 per cent) the SFRs were based on 24 μm, and therefore independent with respect to the SED-based $U - B$ colour.

In this appendix, we re-derive and present the key results from our analysis using the $(\mathrm{NUV} - r) - (r - J)$ diagram to separate

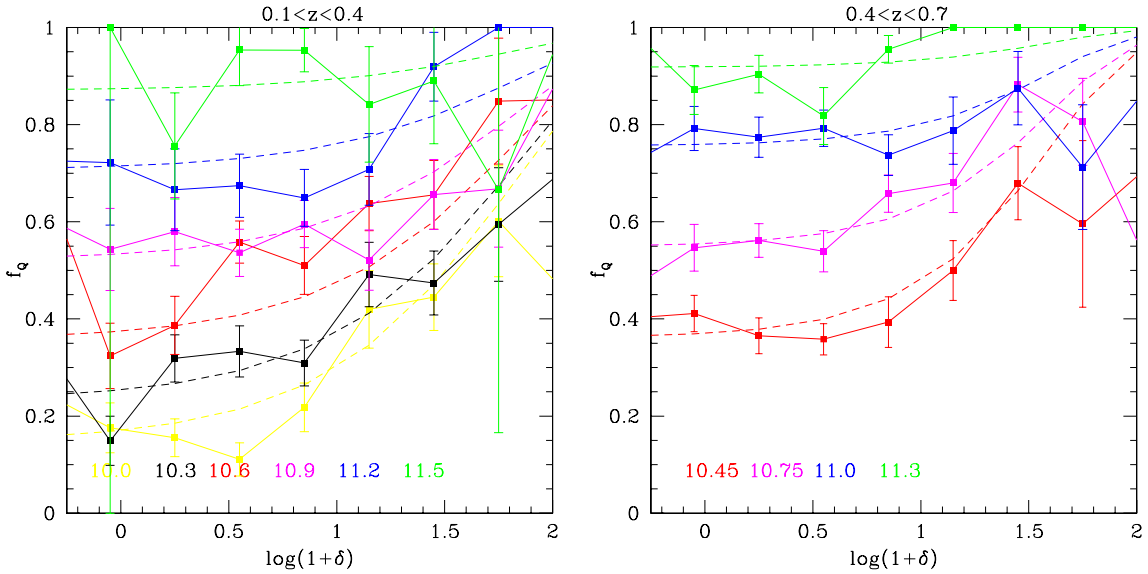

Figure C1. Quiescent fraction as a function of overdensity in different mass bins. Results in the left-hand and right-hand panels are for $0.1 < z < 0.4$ and $0.4 < z < 0.7$, respectively. The measurement points connected by the continuous lines and the dashed curves are for the 0.3 dex bins in stellar mass, with the stellar mass increasing from the bottom to the top. The lowest mass bin starts at the adopted mass-completeness value in that redshift bin, and the rounded values of the centres of the used mass bins are given in the increasing order at the bottom of each panel. The symbols and the continuous lines correspond to the zCOSMOS measurements, and the dashed lines correspond to the best-fitting model given by equation (2) (Section 3.2) when using the $(\mathrm{NUV}-r)-(r-J)$ diagram to identify quenched galaxies. The error bars correspond to half of the 16–84 per cent interval of the ordered quiescent fractions from 100 bootstrapped samples in each redshift bin.

galaxies into active and quiescent populations (similar to Ilbert et al. 2010, 2013). As all the magnitudes are obtained from the same SED fitting described in Section 2.2.2, this is not a completely independent diagnostic with respect to the single $U-B$ colour. However, the colour–colour selection is believed to perform better in separating dusty star-forming galaxies (which may be quite red in $U-B$) from truly quiescent galaxies. As it is used in many different analyses available in the literature (e.g. Bundy et al. 2010; Tinker et al. 2013), it will also enable a quantitative comparison with results from those works. We keep our basic galaxy samples the same as in the main body of the paper, but we calculate new galaxy completeness weights by measuring the completeness in the samples of $(\mathrm{NUV}-r)-(r-J)$ defined active and quiescent galaxies. It turns out that the 30 per cent completeness limits of the zCOSMOS active and quiescent galaxies with respect to the equivalent $I_{AB} < 24$ COSMOS samples is at $\log(M_*/\mathrm{M}_\odot) = 9.81$ and at $\log(M_*/\mathrm{M}_\odot) = 10.28$ in $0.1 < z < 0.4$ and $0.4 < z < 0.7$, respectively. These are almost identical to the values obtained when separating galaxies into red and blue and therefore we have kept the original mass-limits in repeating the analysis.

We show the fraction of colour–colour-defined quenched galaxies as a function of the environmental overdensity in different bins of stellar mass in Fig. C1. This is equivalent to Fig. 3: the points are our results measured in the bins $\Delta\log(M_*/\mathrm{M}_\odot) = \Delta\log(1+\delta) = 0.3$, and the dashed lines correspond to the best-fitting model given by equation (2), where we repeat the fitting in the same intervals adopted in Section 3.2. The agreement between the data and the model shows a similar uncertainty as when using the red fractions. This can be also seen in Fig. C2, where we show the difference between the modelled and measured $(\mathrm{NUV}-r)-(r-J)$ defined quenched fractions in the overdensity–stellar mass plane normalized by the adopted error (half of the 16–84 per cent interval of the ordered quiescent fractions from 100 bootstrapped samples). We conclude that the mass and environment separability holds, within the errors, also when using the colour–colour cut to measure the quenched fraction of galaxies. For reference, we provide the best-fitting $p1-p4$ parameters obtained when separating galaxies in the $(\mathrm{NUV}-r)-(r-J)$ diagram in Table C1.

The quiescent fraction of galaxies as a function of overdensity for centrals and satellites is shown in Fig. C3, where the results are obtained following the analysis in quartiles of overdensity described in Section 4.3. Both samples are matched in stellar mass to the sample of satellite galaxies in the reference overdensity bin. The quiescent fraction of centrals in both redshift bins (blue and cyan squares) is consistent with being independent of the local overdensity, and the corresponding averages (which we adopt to be the quiescent fraction of centrals) and the $\pm1\sigma$ uncertainties are marked with the dashed and dotted lines. The quiescent fraction of satellites in $0.1 < z < 0.4$ (red circles) increases with $\log(1+\delta)$, while in $0.4 < z < 0.7$ (magenta circles) this trend is weaker. However, in both redshift bins the quiescent fraction of satellites is systematically above the quiescent fraction of centrals in a given mass-matched sample. Normalizing this excess of quiescent satellites with respect to centrals by the fraction of star-forming centrals, we obtain the satellite quenching efficiency in the quartiles of overdensity defined by the satellites, shown in Fig. C4. The black continuous line is the $\epsilon_{\mathrm{sat}} = \epsilon_\rho/f_{\mathrm{sat}}$ function expected from our model when the quiescent fraction of centrals is independent of overdensity, showing good agreement with the measured points. For reference, the equivalent ϵ_{sat} functions obtained when using red fractions of galaxies are shown with the dotted lines. The analysis carried out on the quenched fraction of galaxies defined by the two-colour diagram confirms that the satellite galaxies are the main drivers of the observed relations between the quenched fractions and the environmental overdensity $\log(1+\delta)$ in the total population of galaxies at least up to $z = 0.7$.

Overall, the fraction of quenched galaxies defined by the $(\mathrm{NUV}-r)-(r-J)$ diagram is systematically a bit lower than

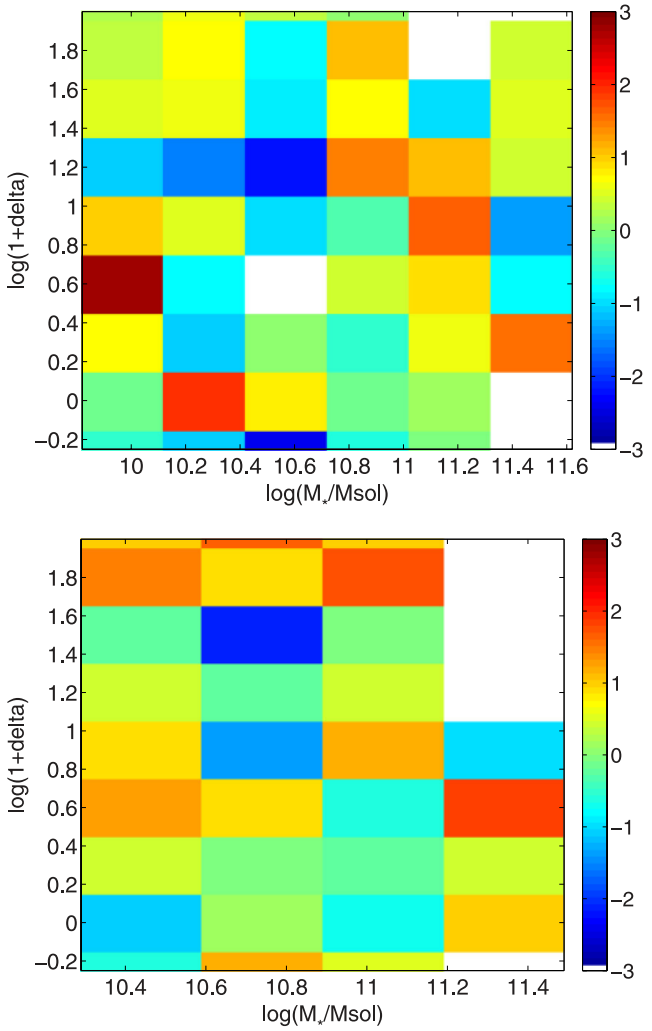

Figure C2. Difference between the modelled and measured quiescent fraction normalized by the adopted error. The obtained values are colour-coded according to the bar shown on the right-hand side. The bins without data are artificially set to have the low negative values (white fields). The top and bottom panels are for the two redshift bins: $0.1 < z < 0.4$ and $0.4 < z < 0.7$, respectively.

when using the $U - B$ cut, as expected if there are some star-forming galaxies appearing as red galaxies in $(U - B)$. However, all the conclusions that are obtained in the main paper when using just a single colour to define the quenched population remain valid.

Table C1. Best-fitting parameters to the $(\mathrm{NUV} - r) - (r - J)$ defined quiescent fraction model.

$z1 < z < z2$	$p1$	$p2$	$p3$	$p4$
$0.1 < z < 0.4$	1.83	0.85	11.05	0.74
$0.4 < z < 0.7$	1.62	1.13	10.86	0.83

The lower z_1 and upper z_2 limits of the redshift bin to which the results refer to are given in the first column, and the best-fitting $p1$, $p2$, $p3$ and $p4$ parameters to the equation (2) when using the $(\mathrm{NUV} - r) - (r - J)$ diagram to separate galaxies to active and quiescent are given in the second to the fifth columns. The fit is obtained with overdensity and mass expressed in $\log(1 + \delta)$ and $\log(M_*/\mathrm{M}_\odot)$ units.

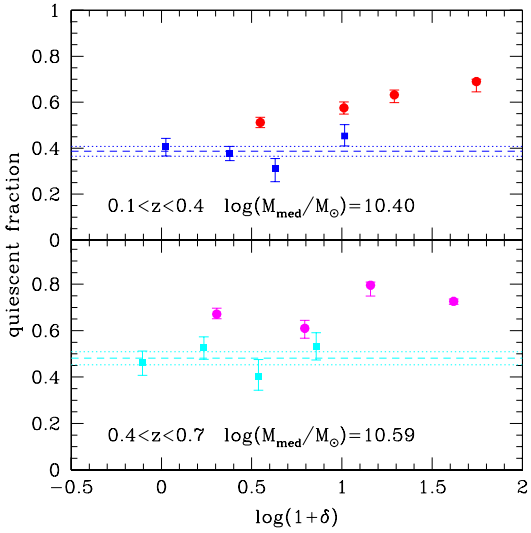

Figure C3. Quiescent fractions of centrals (squares) and satellites (circles) mass-matched to the distribution of satellites in the reference bin as a function of overdensity. Only the purity-corrected quantities are shown, measured at the median stellar mass $\log(M_{\mathrm{med}}/\mathrm{M}_\odot)$ in $0.1 < z < 0.4$ and $0.4 < z < 0.7$ in the top and bottom panels, respectively. The results are plotted at the median overdensity in the bins of overdensity quartiles. The respective errors encompass the 16–84 per cent interval of the purity-corrected quiescent fractions of centrals or satellites in the 20 realizations of the mass matching. The dashed and dotted lines correspond to the average and $\pm 1\sigma$ values of quiescent fraction of centrals.

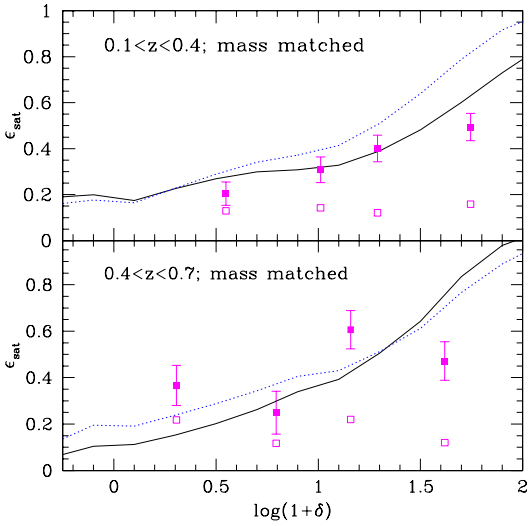

Figure C4. Satellite quenching efficiency ϵ_{sat} as a function of overdensity in $0.1 < z < 0.4$ (top) and $0.4 < z < 0.7$ (bottom) when selecting the quenched population of galaxies using the $(\mathrm{NUV} - r) - (r - J)$ diagram. The symbols are the ϵ_{sat} values measured from the data mass-matched in the quartiles of the satellite overdensity (with median mass $\log(M_*/\mathrm{M}_\odot) = 10.40$ and 10.59 in the lower and higher redshift bins, respectively). The solid and open symbols are for the purity-corrected and -uncorrected quantities, respectively. For clarity, the error bars (encompassing the 16–84 per cent uncertainty interval) are shown only for the former. The black lines correspond to the model prediction $\epsilon_\rho(\delta)/f_{\mathrm{sat}}(\delta, M_*)$ valid in the case when the environmental quenching efficiency of centrals is negligible. For comparison, the dotted blue lines are the $\epsilon_\rho(\delta)/f_{\mathrm{sat}}(\delta, M_*)$ functions obtained when using the $U - B$ colour to identify quenched galaxies.

This paper has been typeset from a TEX/LATEX file prepared by the author.